JOURNAL OF GEOPHYSICAL RESEARCH, VOL. 114, A01210, doi:10.1029/2008JA013697, 2009

Transpolar voltage and polar cap flux during the substorm cycle and steady convection events

Mike Lockwood,[1,2] Marc Hairston,[3] Ivan Finch,[2] and Alexis Rouillard[1,2]

Received 23 August 2008; revised 9 October 2008; accepted 20 October 2008; published 20 January 2009.

[1] Transpolar voltages observed during traversals of the polar cap by the Defense Meteorological Satellite Program (DMSP) F-13 spacecraft during 2001 are analyzed using the expanding-contracting polar cap model of ionospheric convection. Each of the 10,216 passes is classified by its substorm phase or as a steady convection event (SCE) by inspection of the AE indices. For all phases, we detect a contribution to the transpolar voltage by reconnection in both the dayside magnetopause and in the cross-tail current sheet. Detection of the IMF influence is 97% certain during quiet intervals and >99% certain during substorm/SCE growth phases but falls to 75% in substorm expansion phases: It is only 27% during SCEs. Detection of the influence of the nightside voltage is only 19% certain during growth phases, rising during expansion phases to a peak of 96% in recovery phases: During SCEs, it is >99%. The voltage during SCEs is dominated by the nightside, not the dayside, reconnection. On average, substorm expansion phases halt the growth phase rise in polar cap flux rather than reversing it. The main destruction of the excess open flux takes place during the 6- to 10-hour interval after the recovery phase (as seen in AE) and at a rate which is relatively independent of polar cap flux because the NENL has by then retreated to the far tail. The best estimate of the voltage associated with viscous-like transfer of closed field lines into the tail is around 10 kV.

Citation: Lockwood, M., M. Hairston, I. Finch, and A. Rouillard (2009), Transpolar voltage and polar cap flux during the substorm cycle and steady convection events, *J. Geophys. Res.*, *114*, A01210, doi:10.1029/2008JA013697.

1. Introduction

[2] Many publications over many years have demonstrated the relationship between ionospheric transpolar voltage and the electric field (as measured in the Earth's frame of reference) in the interplanetary medium impinging on the magnetosphere [*Reiff et al.*, 1981; *Cowley*, 1981, 1984; *Doyle and Burke*, 1983; *Nishida*, 1983; *Wygant et al.*, 1983; *Reiff et al.*, 1985; *Reiff and Luhmann*, 1986; *Ahn et al.*, 1992; *Boyle et al.*, 1997; *Hairston et al.*, 1998; *Lu et al.*, 2002a, 2002b; *Hairston et al.*, 2003; *Papitashvili and Rich*, 2002; *Shepherd et al.*, 2002; *Bristow et al.*, 2004; *Nakata et al.*, 2004; *Hairston et al.*, 2005; *Ridley*, 2005; *Ruohoniemi and Greenwald*, 2005; *Zhang et al.*, 2007]. These studies, either explicitly or implicitly, assumed steady state conditions because the ionospheric flow pattern and voltage are studied as a function of the prevailing conditions (interplanetary or geomagnetic) with no allowance made for the prior history of those conditions [*Lockwood*, 1991]. For steady state conditions, the interplanetary electric field in the "Stern gap" (the region in undisturbed interplanetary space, outside the bow shock, where field lines are the extensions of open magnetospheric field lines) can be envisaged as mapping down the open field lines to the diameter of the ionospheric polar cap. Averaged over a sufficiently long interval, the magnetosphere is well described by steady state and this is a valid concept; however, on shorter timescales the time derivatives of the magnetic field B mean that the electric field is not curl-free and the steady state mapping does not apply [*Lockwood et al.*, 1990; *Lockwood and Cowley*, 1992; *Cowley and Lockwood*, 1992]. The concept of the accumulation and loss of open flux in the magnetosphere (which therefore inductively decouples interplanetary electric fields from ionospheric ones) is central to our knowledge of the substorm cycle [e.g., *Holzer et al.*, 1986]. *Russell* [1972] first sketched the forms of the ionospheric convection patterns that must apply on timescales shorter than the duration of substorm cycles. However, an understanding of how one can reconcile the different reconnection voltages in the magnetopause (where open field lines are produced) and in the cross-tail current sheet (where open field lines are destroyed), with the incompressible nature of ionospheric flow was first provided by *Siscoe and Huang* [1985] who introduced the concept of moving "adiaroic" (meaning "not flowing across") polar cap boundaries between the dayside and nightside merging gaps (the ionospheric

[1]Space Environment Physics, School of Physics and Astronomy, Southampton University, Southampton, UK.
[2]Space Science and Technology Department, Rutherford Appleton Laboratory, Didcot, UK.
[3]W. B. Hanson Center for Space Sciences, University of Texas, Richardson, Texas, USA.

0148-0227/09/2008JA013697$09.00

projections of the reconnection X lines). Analytic models predicting the pattern of flow for unbalanced dayside and nightside reconnection voltages (i.e., non-steady state) have now been developed by *Freeman* [2003] and by *Lockwood and Morley* [2004] but are restricted to the simplification that the region of open field lines always remains circular [see also *Lockwood et al.*, 2006]. *Cowley and Lockwood* [1992] discussed conceptually how, in this "Expanding-Contracting Polar Cap" (ECPC) model of ionospheric convection, it is not the mapped interplanetary magnetic field which drives ionospheric convection: rather it is the production and destruction of open field lines by magnetopause and tail reconnection (at rates given by voltages Φ_D and Φ_N, respectively). While Φ_D is directly related to the interplanetary electric field (which determines the magnetic shear across the dayside magnetopause), Φ_N is dependent on the magnetic shear across the relevant portion of the cross-tail current sheet, and so is only very indirectly related to the solar wind electric field.

[3] The ECPC model has the potential to explain the very considerable scatter in the plots of transpolar voltage as a function of interplanetary electric field [e.g., *Cowley*, 1981; *Bristow et al.*, 2004]. In many studies, this scatter has been reduced by selecting intervals in which the interplanetary electric field is exceptionally steady. The practical reason for doing this is that uncertainties in the propagation delay from the solar wind monitor to the ionosphere are not a source of error. However, this practice also means that intervals approaching more steady state situations will tend to have been selected and these will show less scatter because Φ_D and Φ_N are more closely matched. The predictions of the ECPC model for transpolar voltage are discussed further in section 2. The implications of assuming steady state (and so wrongly assuming the transpolar voltage Φ_{PC} is the same as the dayside reconnection voltage Φ_D) have also been discussed recently by *Milan et al.* [2007].

[4] The effects of polar cap expansion and contraction on ionospheric flow patterns and transpolar voltages has been discussed by several authors in a number of case studies [*Lockwood et al.*, 1990, 2006; *Lockwood*, 1991; *Lockwood and Cowley*, 1992; *Freeman et al.*, 1993; *Grocott et al.*, 2002; *Milan*, 2004; *Milan et al.*, 2007, 2008]. In addition, because the nightside reconnection voltage Φ_N is enhanced during substorm expansion and recovery phases it is associated with the AL index and several studies have noted the strong effect of AL on statistically derived patterns of ionospheric convection and on transpolar voltage [*Ahn et al.*, 1992, 1995; *Weimer*, 1999, 2001; *Provan et al.*, 2004; *Cai et al.*, 2006].

[5] The dual-source nature of the main flow excitation in the ECPC model introduces a number of distinct timescales into the response of the transpolar voltage to IMF changes. Indeed, it was this feature that lead to the confirmation and development of the ECPC model, following the advent of ground-based radars with the ability to monitor convection changes on timescales considerably shorter than the orbital period of ionospheric satellites [*Freeman and Southwood*, 1988; *Lockwood and Cowley*, 1988; *Lockwood and Freeman*, 1989]. The first timescale is the response time of the dayside flows to the onset of a magnetopause reconnection voltage [*Lockwood and Cowley*, 1988; *Lockwood et al.*, 1990; *Ruohoniemi and Greenwald*, 1998]. This is followed by a more gradual change in the flow pattern as the polar cap expands during the subsequent substorm growth phase [*Hairston and Heelis*, 1995; *Khan and Cowley*, 1999; *Lu et al.*, 2002a, 2002b], a feature which is very well reproduced by the numerical implementation of the ECPC model by *Morley and Lockwood* [2005]. The third timescale is the duration of the growth phase after which AL decreases rapidly and the nightside reconnection voltage is enhanced. As well as being seen in flow responses detected by radars and magnetometers [e.g., *Grocott et al.*, 2002], these timescales have been detected in transpolar voltage data [e.g., *Eriksson et al.*, 2001].

[6] We also here note a further complication in the relationship between the interplanetary electric field and the transpolar voltage, namely the "saturation" phenomenon which occurs when the electric field becomes very large. Under these conditions, the transpolar voltage asymptotically tends toward a maximum value [*Hairston et al.*, 2003, 2005; *Nagatsuma*, 2004; *Ridley*, 2005]. This effect introduces nonlinearity into the relationship between ionospheric voltages and the interplanetary electric field. The mechanisms proposed for this effect generally involve a limitation to the growth of the dayside reconnection voltage as the polar cap flux increases [*Siscoe et al.*, 2004; *Kivelson and Ridley*, 2008]. The implications for the saturation phenomenon of the results presented in the present paper are investigated in the follow-up paper (M. Lockwood et al., Polar cap voltage and flux saturations, submitted to *Geophysical Research Letters*, 2008; hereinafter referred to as Lockwood et al., submitted manuscript, 2008).

[7] The transpolar voltage has been measured in three main ways: (1) by integrating the observed electric field along an orbit of a spacecraft traversing the polar cap [e.g., *Hanson et al.*, 1993; *Hairston et al.*, 1998]; (2) via data mapping techniques such as AMIE (Assimilative Mapping of Ionospheric Electrodynamics [e.g., *Lu et al.*, 1994, 2002a, 2002b; *Ridley*, 2005; *Kihn et al.*, 2006]) which use input from many sources (magnetometers, radars and satellites); and (3) using a model fit to line-of-sight velocities deduced from the SuperDARN network of HF radars [e.g., *Ruohoniemi and Greenwald*, 2005]. There are advantages and disadvantages to all three. The two mapping techniques (AMIE and SuperDARN "mapped potential") give a full spatial convection pattern and so the largest voltage can be selected rather than that along a certain satellite pass: this also puts the voltage value in the context of the whole pattern. The transpolar voltage values can also be obtained at higher time resolution using these mapping techniques (down to 90 sec.) whereas for the satellite data the voltage measurement takes several minutes and is repeated only roughly 45 min later in the polar cap of the opposite hemisphere. The disadvantages of the mapping techniques are that boundaries tend to be highly smoothed and that it is very difficult to assess the effect that the model used, as opposed to the data input, has had on the derived voltage.

[8] A number of studies have used the mapping techniques, often allied with global auroral images, to derive both the dayside an nightside reconnection voltages separately by defining the open-closed boundary (and how it is moving) and hence the flow of plasma and frozen-in magnetic flux across it in its own rest frame [*Lockwood and Cowley*, 1992;

Hubert et al., 2006; *Milan et al.*, 2007, 2008]. The main difficulty with this technique is that the open-closed boundary can be very difficult to define and can sometimes be considerably removed from readily detectable boundaries in global auroral images [see review by *Chisham et al.*, 2008].

[9] We here use direct satellite measurements in a statistical survey. For the data set employed (see section 3), the craft traverses the polar cap with a distribution of traveltimes varying between 0.2 min and 22.9 min., with mean and median values both equal to 6.7 min (note that the very short duration passes are generally close to tangential to the polar cap boundary and are removed by the orbit selection criteria we apply in section 4). The orbital period is 105 min. and in that time the satellite traverses the polar caps of both hemispheres. The exact path of the polar cap traversal varies. In this paper, we place restrictions on the orientation of the satellite paths employed (see section 5) which result in the full sample of 10,216 polar cap passes obtained in one year [2001] being reduced to a set of 9627 passes. These passes cover the dayside and nightside polar cap and are used to assess statistically the changes in the convection polar cap magnetic flux. Web subsequently place a further restriction on the position of a pass such that it traverses the center of the polar cap which further reduces the data set to 2313 passes.

[10] In the next section, we use the ECPC model to formulate a procedure for fitting the data and in section 4 we devise a classification scheme to allow the data to be used to study the effect of substorm phase. Section 6 describes a novel method for estimating the polar cap flux statistically. The results are presented in sections 7–9, with discussion and conclusions in sections 10 and 11.

2. Expanding-Contracting Polar Cap Model

[11] The ECPC model applies Faraday's law to the open/closed field line boundary to give the rate of change of open magnetic flux [*Siscoe and Huang*, 1985]:

$$dF_O/dt = B_i(dA_O/dt) = \Phi_D - \Phi_N \quad (1)$$

where Φ_D is the reconnection voltage along the X line in the dayside magnetopause (where geomagnetic field lines are opened) and Φ_N is the voltage along the X line in the cross-tail current sheet where open field lines are closed again. The ionospheric field strength B_i is close to constant and so equation (1) gives the rate of change of A_O, the polar cap area (here defined as the region of open magnetic flux). Steady state conditions ($dF_O/dt = 0$) therefore require $\Phi_D = \Phi_N$. The more general cases of $\Phi_D > \Phi_N$ (substorm growth phases) and $\Phi_D < \Phi_N$ result in polar cap expansion and contraction, respectively. *Lockwood and Cowley* [1992] found $\Phi_D < \Phi_N$ in both the expansion and recovery phases of the one substorm that they studied, but the generality of this is investigated in the present paper. In these nonsteady situations, an ionospheric electric field (in the Earth's frame of reference) is seen away from the ionospheric projections of the X lines (the "merging gaps"): between the merging gaps are the adiaroic boundaries where no field lines are crossing the open-closed boundary (i.e., they do not map to active reconnection X lines) but an electric field exists in the Earth's frame because those adiaroic boundaries are in motion. *Lockwood* [1991] noted that for the highly idealized case where the polar cap remains circular at all times, the ionospheric electric field associated with the difference $|\Phi_D - \Phi_N|$, and hence with the polar cap expansion or contraction, is distributed uniformly around the polar cap boundary, i.e., it has a magnitude of $|\Phi_D - \Phi_N|/(2\pi r_{PC})$ where r_{PC} is the polar cap radius: this means that a spacecraft travelling from dawn to dusk, or in the opposite direction, which intersects the ends of the dayside merging gap will, for a circular polar cap, see a reconnection voltage of $\Phi_D - L_D(\Phi_D - \Phi_N)/(2\pi r_{PC})$ and one which intersects the ends of the nightside merging gap will detect $\Phi_N - L_N(\Phi_N - \Phi_D)/(2\pi r_{PC})$ where L_D and L_N are the lengths of the dayside and nightside merging gaps. In effect, some of the applied magnetospheric voltages Φ_N and Φ_D cause a motion of the open-closed boundary rather than driving flow in the Earth's frame and the voltage seen in the Earth's frame is lower than the applied voltage. A pass which intersects the center of this circular polar cap, but passes through the two adiaroic segments of the cap boundary (for which the separation of the boundary crossing points along the boundary is $L = \pi r_{PC}$), will see a reconnection-driven voltage of $\Phi_D - \pi r_{PC}(\Phi_D - \Phi_N)/(2\pi r_{PC}) = 0.5(\Phi_D + \Phi_N)$ [*Lockwood*, 1991]. In general we need to add to this Φ_V, the sum of the voltage on the two flanks of the magnetosphere driven by any viscous-like (nonreconnection) process [*Milan*, 2004; *Newell et al.*, 2008]:

$$\Phi_{PC} = 0.5(\Phi_D + \Phi_N) + \Phi_V \quad (2)$$

[12] The viscous-like voltages (and other features such as ionospheric conductivity gradients) also cause the convection reversal boundary to generally lie equatorward of the open-closed field-line boundary [*Siscoe et al.*, 1991; *Lockwood*, 1997] which means that the flux in the convection polar cap, F_{PC}, is slightly larger than the open flux region, F_O.

[13] Equation (2) holds at all times, as long as the polar cap remains circular as it expands and contracts and the satellite intersects its center. In general, the satellite will not pass through this central point and the polar cap expansion/contraction will not be uniform so equation (2) must be generalized to

$$\Phi_{PC} = c\Phi_D + d\Phi_N + \Phi_V \quad (3)$$

where c and d vary from pass to pass and depend on the evolution of the polar cap shape. If we assume magnetic shear to determine reconnection voltage we expect Φ_D to be proportional to ε^*, the modified epsilon which gives the dawn-dusk electric field in the magnetosheath which depends on an IMF parameter such as $B\sin^4(\theta/2)$ (where B is the IMF field strength and θ is the IMF clock angle in the GSM ZY frame) and the amplification of B in the magnetosheath by the draping of field lines over the nose of the magnetosphere. Likewise, we expect Φ_N to be proportional to the field B_{TLX} in the tail lobe at the location of the tail X line responsible for closing open field lines. Because the tail lobe flux contains both open and closed field lines (taken into the tail and polar cap by the voltages Φ_D and Φ_V, respectively) we expect B_{TLX} to depend on F_{PC},

rather than F_O (although, because Φ_V is small, we expect the flux in the tail lobe dragged there by viscous-like interaction, ($F_{PC} - F_O$), to be relatively small). However this dependence on F_{PC} varies greatly with the position of the tail X line. For a very distant X line, sufficiently far down the tail that the flaring angle has fallen to zero, B_{TLX} is set by pressure balance with the static pressure in the interplanetary medium and is independent of the polar cap flux, F_{PC} (increasing F_{PC} causes the tail to increase in cross-sectional area, i.e., to flare, but B_{TLX} remains constant). However, for an X line closer to the Earth, the tail flaring angle is not zero and the solar wind dynamic pressure does not allow the tail to flare unhindered. Thus we can write (3) as

$$\Phi_{PC} = a\,\varepsilon^* + bF_{PC}^n + \Phi_V \quad (4)$$

where the values of a and b will depend on the pass and polar cap geometry (via the factors c and d in equation (3)) but also on the "constants" of proportionality with the magnetic shears, which could depend on other parameters (such as the solar wind speed, dynamic pressure, static pressure, Mach number, etc.) [e.g., *Boudouridis et al.*, 2007]. For a linear system the factor a would be independent of the state of the magnetosphere (and hence the substorm phase); however we note that the theories of voltage saturation predict that a falls with increasing F_O [*Siscoe et al.*, 2004] and hence increasing F_{PC}. However, the factor b will certainly depend on the position of the tail X line and hence on substorm phase: during growth and late recovery phases the tail X line will be far from Earth and we would expect b to be small because increasing F_{PC} would mainly cause the tail at the (far) X line to flare and would only weakly increase the magnetic shear across the X line. We would expect a significant rise in b shortly after substorm onset, when the Near-Earth Neutral Line (NENL) pinches off the plasmoid and starts to close open flux: this is because a NENL would have a stronger dependence on F_{PC} because the tail is less able to flare at an NENL than it is at a far X line. Hence changing F_{PC} has a large effect on the magnetic shear ($2B_{TLX}$) at an NENL. However this effect would be reduced at greater distances down the tail (smaller b) and entirely absent ($b = 0$) for a sufficiently distant "far X line".

[14] To reduce the effects of variability of c and d in equation (4) we here select passes close to the dawn-dusk meridian. The effects of changes in the polar cap shape, however, will remain and here are averaged out for a given substorm phase by using an ensemble of many passes.

3. Data Sets Employed

[15] We here employ measurements of the transpolar voltage from the cross-track drift of plasma measured by the topside ionospheric Defense Meteorological Satellite Program (DMSP) F-13 satellite. This drift gives the along-track electric field which can be integrated to give the distribution of electric potential along the orbit. The difference between the maximum and minimum potential is the transpolar voltage, Φ_{PC}. F-13 was chosen because it traverses the polar cap close to parallel to the 06-18 MLT meridian. The data for the full calendar year 2001 were used because it was near solar maximum and hence of disturbed geomagnetic conditions. In addition, at sunspot maximum the greater scale height of the topside ionosphere maintains the fraction of O^+ ions which means the instruments operate under optimum conditions, giving continuous, high-quality transpolar voltage data. Including northern and southern hemisphere passes, this data set contained a total of 10,216 polar cap traversals. The orbit of F-13 means that the northern hemisphere passes tend to sample the dayside polar cap whereas those in the southern hemisphere favor the nightside polar cap.

[16] The data were compared with the AE (Auroral Electrojet) indices, AU and AL, and with IMF and solar wind values from the 5-minute Omni data set. These interplanetary data have been propagated from the monitoring spacecraft to the nose of Earth's bow shock, using a minimum variance technique to determine the orientation of solar wind/IMF structures [*King and Papitashvili*, 2005]. Cross-correlation analysis with the transpolar voltage set revealed that there was an additional 5-minute delay on average from the bow shock to the dayside polar ionosphere. The variance in the estimated satellite-to-ionosphere propagation delay was used to evaluate the maximum and minimum values, within the lag uncertainty interval, of the solar wind speed V_{SW} and of the IMF parameters B_z and $B\sin^4(\theta/2)$. Because the autocorrelation time of V_{SW} is much greater than for the IMF parameters [*Lockwood*, 2002a], its uncertainty due to possible propagation delay errors is generally much smaller than those for the IMF parameters.

4. Classification of Substorm Phases, Quiet Periods, and Steady Convection Events

[17] Figure 1 shows an example of a plot which was produced for all 10,216 polar cap passes by F-13 during 2001. It covers an approximately half-day interval on day number 123 of 2001, from 05:06:13 UT to 17:22:33 UT. The period 9:17:57–9:25:05 UT (between green and red vertical lines in panels a to c) covers a single polar pass of F-13 across the southern hemisphere polar cap. This pass was during the growth phase of an isolated substorm. From top to bottom, Figure 1 shows: the solar wind velocity, V_{SW}; the IMF B_Z component in the GSM frame; the AE indices AU (blue) and AL (red); the transpolar voltage measured by F-13, $\Phi_{PC;}$ the estimated convection polar cap flux F_{PC} (see section 6); the IMF $B\sin^4(\theta/2)$ parameter; and the AL index. The parameters in Figures 1d–1g are sampled at the times of the polar cap traversals, in the case of the IMF data, allowing for the estimated satellite-to-ionosphere propagation lag. These polar cap traversals are alternately for the southern and northern hemisphere polar caps. The phases of the substorm are divided by the vertical black lines and are classified using the following definitions:

[18] C = 1: Quiet with AL > −100 nT and Φ_{PC} < 60 kV and AU < +50 nT and more than 1 hr. after a period of class 5 (C = 5 being a substorm/steady convection event [SCE] recovery phase).

[19] C = 2: Substorm growth phase: indicated by a small rise in AU but AL still exceeding −100 nT. Must also be within 3hr. of a substorm expansion seen in AL (i.e., must be followed by a period classed as C = 3). Often the start of the growth phase is better identified by a negative swing in IMF B_z than by the start of the rise in AU.

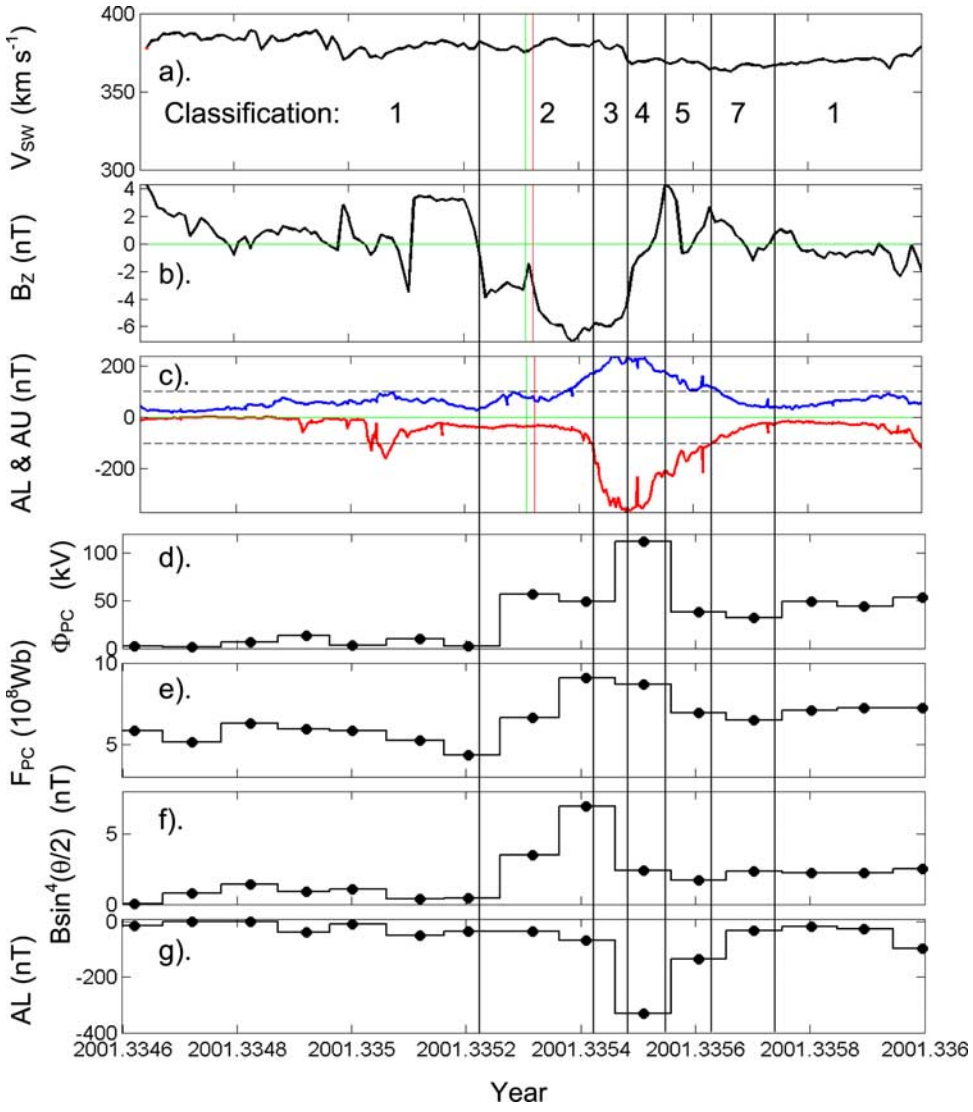

Figure 1. (a) Analysis of conditions during an example 12-hour interval around a southern hemisphere polar cap pass by DMSP F-13 on day number 123 of 2001 at 9:17:57–9:25:05 UT (between green and red vertical lines). This pass was during the growth phase of an isolated substorm. From top to bottom: the solar wind velocity, V_{SW}; the IMF B_Z component in the GSM frame; the AE indices AU (blue) and AL (red); the transpolar voltage measured by F-13, Φ_{PC}; the estimated convection polar cap flux F_{PC} (see text for details); the IMF $B\sin^4(\theta/2)$ parameter; and the AL index sampled at the time of the pass. The IMF data are lagged as described in the text. The points in Figures 1d–1g are for the times of the traversal between the polar cap potential minima and maxima: These polar cap traversals are alternately for the southern and northern hemisphere. The phases of the substorm are divided by the vertical black lines and are classified as 1 = quiet, 2 = growth phase, 3 = prepeak expansion phase, 4 = postpeak expansion phase, 5 = recovery phase, and 7 = quiet postrecovery.

[20] C = 3: Prepeak expansion phase: requires AL < −100 nT but before the minimum AL is reached.

[21] C = 4: Postpeak expansion phase: requires AL < −100 nT and must immediately follow a minimum in AL and a period of class 3. This phase ends (and becomes C = 5, the recovery phase) when AL increases past a threshold halfway between the minimum value and the quiet −100 nT threshold.

[22] C = 5: Recovery phase starts at the end of a period of either class 4 or class 6, when AL increases past halfway between its minimum value (at the boundary between phases 3 and 4) and the quiet −100 nT threshold. It ends when AL returns to exceeding −100 nT.

[23] C = 6: Steady convection event: if a period of class 3 is not followed within 2 hr. by clear intervals of class 4 and then 5, it is classed as a steady convection event until the criterion for the start of a recovery phase (class 5) is met.

[24] C = 7: A period that meets the quiet AL criterion (>−100 nT) but is within 1 hour of a recovery phase (class 5).

[25] Also, in subsequent sections we use some combinations of classifications such as quiet and growth (C = 1 & 2), disturbed AL (C = 3, 4, 5 & 6) and substorm (C = 3, 4, & 5).

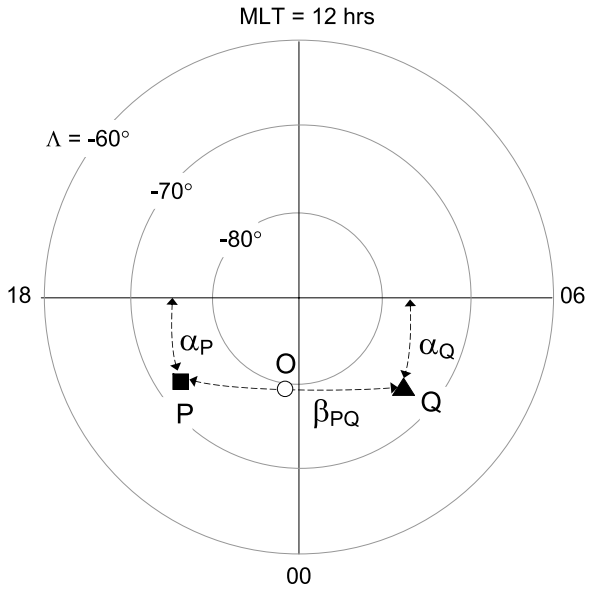

Figure 2. MLT-invariant latitude (Λ) plot of the orbit of DMSP F-13 during the southern polar cap traversal on day number 123 of 2001 at 9:17:57–9:25:05 (between the green and red vertical lines in Figure 1). The solid square is the point P where F-13 encountered the minimum potential $\Phi_P = -29.77$ kV at invariant latitude $\Lambda_P = -73.26°$ and $[MLT]_P = 20.30$ hours. The solid triangle is the point Q where F-13 encountered the maximum potential $\Phi_Q = +27.43$ kV at $\Lambda_Q = -73.66°$ and $[MLT]_Q = 3.29$ hours. The open circle O is where F-13 crossed the zero potential contour. The angular length of the great circle separation of PQ (subtended by P and Q at the Earth's center) is β_{PQ}. For this example of a polar cap traversal, $\beta_{PQ} = 26.39°$. P and Q were separated from the closest approach of the 01-18 MLT meridian by great circle angular distances of α_P and α_Q, respectively. Passes close to parallel with the 06-18 MLT meridian are here selected using $|\alpha_P - \alpha_Q| \leq 2°$ and their position in the noon-midnight direction characterized by $\alpha = (\alpha_P + \alpha_Q) / 2$. Values of α are defined as positive sunward of the 06-18 MLT meridian, and this pass gave $\alpha_P = -9.40°$ and $\alpha_Q = -10.56°$ (and hence $\alpha = -9.98°$). The observed transpolar voltage in this case was $\Phi_{PC} = \Phi_Q + |\Phi_P| = 57.20$ kV.

[26] The example pass selected in Figure 1 shows that it was during the growth phase of an isolated substorm. By the above criteria, the pass at the plot center was classed as 2, and was in a sequence of passes shown classed 1,1,1,1,1,1,1,2,2,4,5,7,1,1,1 (i.e., for this isolated substorm the phase classed 3 was short and missed between passes). Note that F-13 sampled the substorm growth phase in both hemispheres, the postpeak expansion phase in the southern and the recovery phase in the northern. Figures 1d–1g show values derived from the satellite data from the polar traversals and means of supporting data for the duration of the traversal (in the case of the IMF data, they are averaged over the interval allowing for the propagation delay from the satellite to the ionosphere). The IMF $B\sin^4(\theta/2)$ parameter increased during the growth phase following the southward turning at its start, and then decreased with a northward turning late in the expansion phase. The transpolar voltage Φ_{PC} was about 40 kV higher during the growth phase than in the preceding quiet interval but then increased to over 100 kV in the expansion phase. The polar cap flux F_{PC} (derived in section 6) increased during the growth phase and then decreased again in the expansion and recovery phases. After this substorm, $B\sin^4(\theta/2)$, Φ_{PC} and F_{PC} were all higher than they were during the quiet interval before the growth phase.

[27] We note that in the past individual studies have selected different definitions of the substorm phases. The above definition set is somewhat tailored to the present study because the transpolar voltage Φ_{PC} is used (to define quiet periods), as well as the more readily available data AU, AL and IMF B_z. Had it existed, we would have employed an agreed standard set of definitions which would allow comparison with other studies. We suggest that it would be a very useful step for a body, probably under the auspices of ICSU, to research and agree a set of substorm phase definitions which could be readily generated for both past and future data sets.

5. Classification of Satellite Pass Geometry

[28] Figure 2 describes the path of DMSP F-13, in an MLT-invariant latitude (Λ) frame, during the polar cap traversal at the center of the period studied in Figure 1. The solid square is the point P where F-13 encountered the minimum potential $\Phi_P = -29.77$ kV. The solid triangle is the point Q where F-13 encountered the maximum potential $\Phi_Q = +27.43$ kV. The open circle O is where F-13 crossed the zero potential contour. The angular length of the great circle separation of PQ (subtended by P and Q at the Earth's center) is β_{PQ}. For this example of a polar cap traversal, $\beta_{PQ} = 26.39°$. P and Q were separated from the relevant closest approaches of the 06-18 MLT (dawn-dusk) meridian by great circle angular distances of α_P and α_Q, respectively. Passes that were close to parallel with the 06-18 MLT meridian are selected using $|\alpha_P - \alpha_Q| \leq 2°$ and their position in the noon-midnight direction characterized by $\alpha = (\alpha_P + \alpha_Q) / 2$. Values of α are defined as positive sunward of the 06-18 MLT meridian, and this pass had values $\alpha_P = -9.40°$ and $\alpha_Q = -10.56°$ and hence $\alpha = -9.98°$. The observed transpolar voltage in this case was $\Phi_{PC} = \Phi_Q + |\Phi_P| = 57.20$ kV.

6. Estimation of the Convection Polar Cap Flux

[29] The use of the parameter α enables us to evaluate the behavior of the whole polar cap in a statistical manner. The total of 10,216 polar cap traversals by the DMSP F-13 during 2001 varied in their α value between 18.021° and −24.822°. Of these, 9627 passes meet the criterion $|\alpha_P - \alpha_Q| \leq 2°$. These were sorted into eight bins of α, each 5° wide. For each of these bins, the distribution of the angular widths of the convection polar cap β_{PQ} was evaluated. The orbit of F-13 is such that the dayside ($\alpha > 0$) passes tend to occur in the northern hemisphere whereas the nightside ($\alpha < 0$) passes tend in the south. Figure 3 shows the cumulative probability distributions of the angular separation between P and Q exceeding any given value β_{PQ}, $P[\beta > \beta_{PQ}]$. Note that for passes with large $|\alpha|$ the satellite may not intersect the polar cap at all (especially if the polar cap is small):

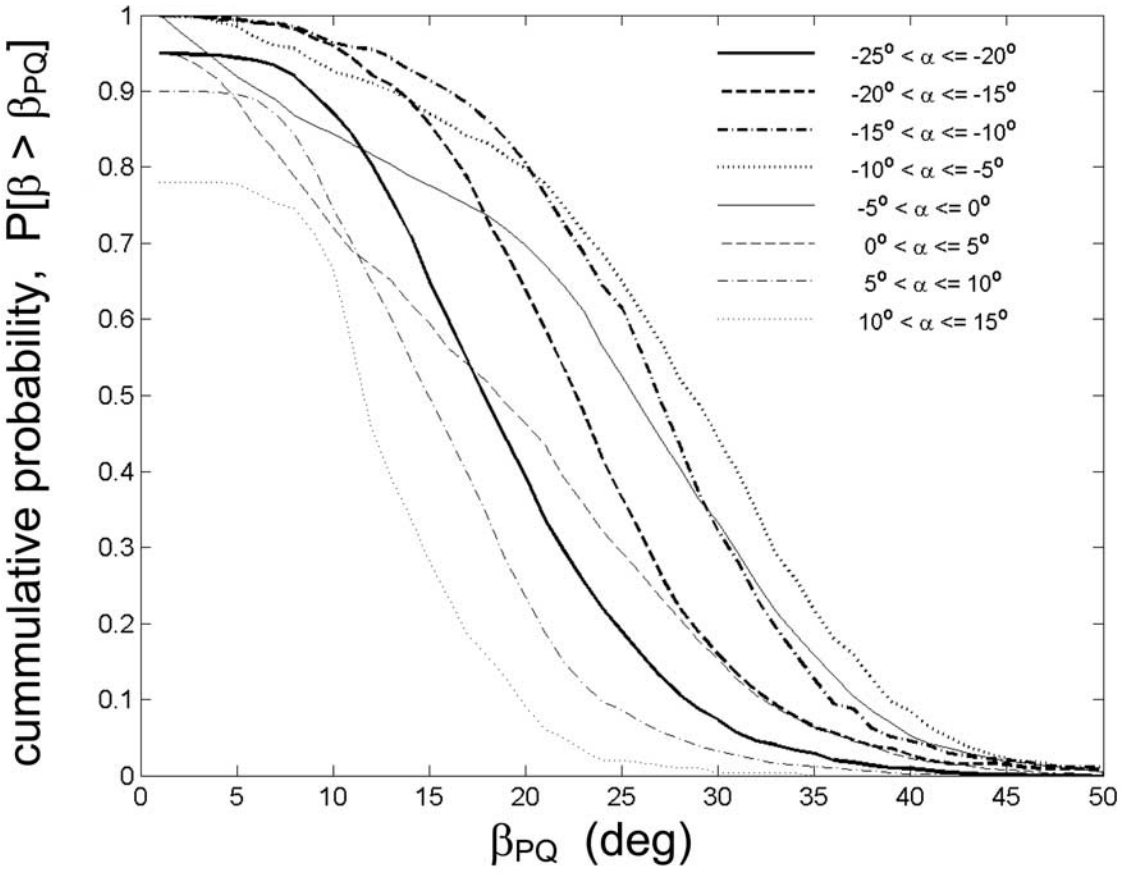

Figure 3. Cumulative probability distributions of β_{PQ} (see Figure 2) for various ranges of α (the noon-midnight position parameter of the pass). $P[\beta > \beta_{PQ}]$ is the probability that the angular separation between P and Q exceeds the threshold β_{PQ}. The data used are the 9627 polar cap traversals by the DMSP F-13 during 2001 (which vary in α between 18.021° and −24.822°) and meet the criterion $|\alpha_P - \alpha_Q| \leq 2°$. These are divided into the eight 5° ranges of α shown.

these passes are included in these distributions with $\beta_{PQ} = 0$. The distribution is given for each of the 8 bins of α in Figure 3. The variation of the angular polar cap diameter β_{PQ} is shown as a function of the noon-midnight position parameter of the pass, α, in Figure 4. The gray points give the β_{PQ} and α values of the 9627 DMSP F-13 polar cap traversals that meet the criterion $|\alpha_P - \alpha_Q| \leq 2°$, the black points are where $P[\beta > \beta_{PQ}]$ equals thresholds of 0.1 to 0.9 in 0.1 increments, scaled from Figure 3. For each α range these points are plotted by the mean α value for all the passes in that range. The solid lines are 5th-order polynomial fits to the black points for each probability threshold. These lines give a statistical view of the variation of the size and shape of the polar cap. We here assume that if we have a convection polar cap area that has a cumulative probability of x (i.e., it is exceeded for a fraction x of the time), then the $P[\beta > \beta_{PQ}]$ value at all α values is also x. This does not allow for any systematic shifts of the polar cap in the sunward/antisunward direction, but because of the way β_{PQ} is derived, the results would not be affected by polar cap shifts in the dawn-dusk direction. The shape of the boundaries is interesting. The curve in Figure 4 for $P[\beta > \beta_{PQ}] = 0.9$ is the closest to circular with the largest polar cap diameter at α near −5°. As the $P[\beta > \beta_{PQ}]$ falls, the dayside polar cap width falls faster than the nightside and a more *"teardrop"* shape emerges, reminiscent of the polar cap shape during *"horse-collar"* aurora that are frequent during intervals of northward IMF [*Murphree et al.*, 1982; *Hones et al.*, 1989]. Figure 4 shows a band of frequent occurrence of passes (revealed by the higher density of gray points) between the sunward limit of southern hemisphere passes and the antisunward limit of northern hemisphere passes. Studying this band reveals no systematic difference between north and south hemisphere and so combining the dayside data (derived mainly from northern hemisphere passes) and the nightside data (mainly from the southern hemisphere) is not a major problem.

[30] The total area inside each of the contours of constant $P[\beta > \beta_{PQ}]$ can be calculated by integrating the area of each strip across the full range of α, $A_{PC} = \int_\alpha r\beta_{PQ}\, r d\alpha$, where r is the geocentric height of the satellite. Thus we can compute the convection polar cap flux

$$F_{PC} = B_i \int_\alpha \beta_{PQ}\, r^2\, d\alpha \qquad (5)$$

where B_i is the ionospheric magnetic flux density (taken to be constant at 5×10^{-5} T). The points in Figure 5 are the convection polar cap flux F_{PC} computed using equation (5)

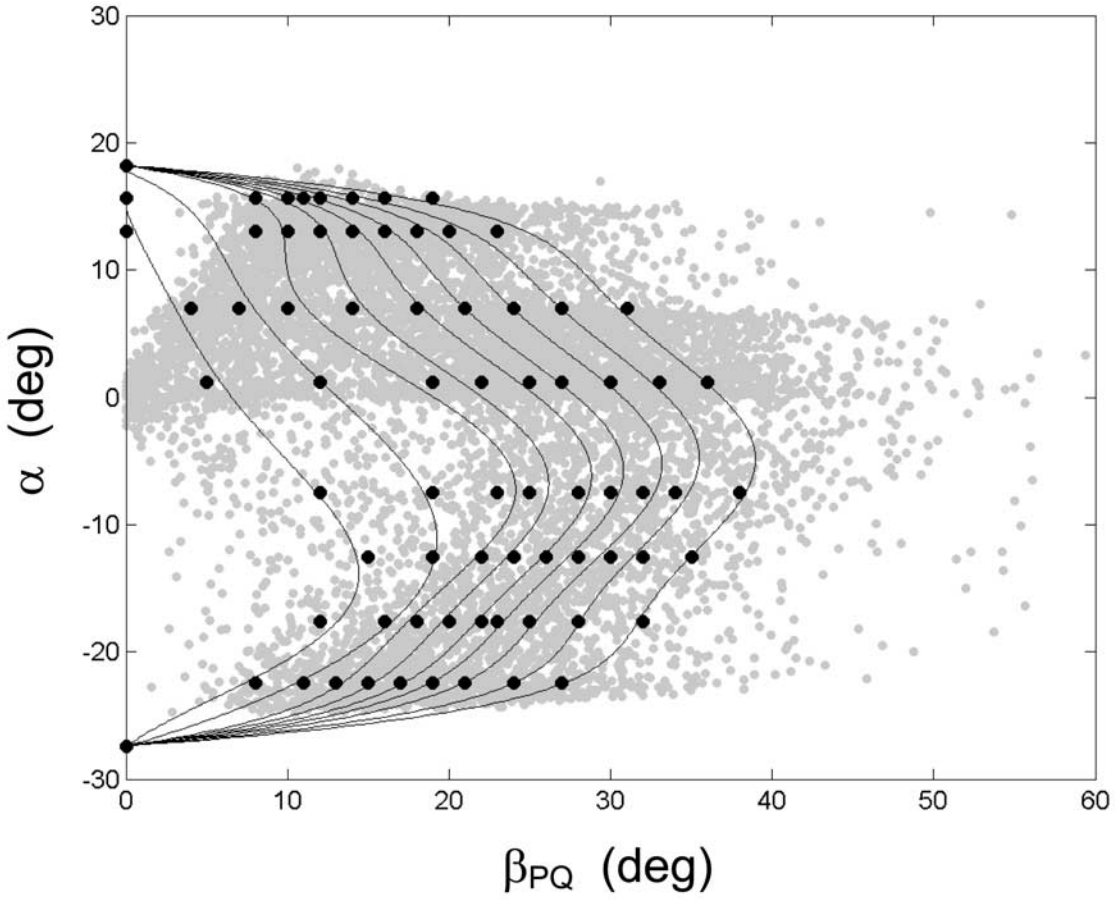

Figure 4. Scatterplot (gray dots) of the angular polar cap diameter β_{PQ} (x axis) as a function of the noon-midnight position parameter, α, of the pass (y axis) for the 9627 DMSP F-13 polar cap traversals that meet the criterion $|\alpha_P - \alpha_Q| \leq 2°$. Each horizontal line of solid black points show where the cumulative probabilities $P[\beta > \beta_{PQ}]$ (see Figure 3) exceed thresholds of (from right to left) 0.1 to 0.9 in increments of 0.1 within the ranges of α used in Figure 3. They are plotted at the mean value for the α ranges. The solid lines are 5th-order polynomial fits to the black points for each probability threshold.

for the nine contours of constant $P[\beta > \beta_{PQ}]$ in Figure 4. In addition, we can add a point at $F_{PC} = 0$ and $P[\beta > \beta_{PQ}] = 1$. The solid line is a 5th-order polynomial fit to the solid points. This curve is used to convert the observed angular polar cap diameter β_{PQ} into a statistical convection polar cap flux estimate F_{PC}, by evaluating the probability that the observed β_{PQ} value is exceeded at the α of the pass, $P[\beta > \beta_{PQ}]$, and then scaling the F_{PC} value for that $P[\beta > \beta_{PQ}]$. As discussed above, this assumes that the convection polar cap shrinks and expands, not in a shape-preserving manner, but so that the $P[\beta > \beta_{PQ}]$ value is independent of α.

[31] Thus from evaluation of its $P[\beta > \beta_{PQ}]$ value at the α of the pass, the polar cap flux F_{PC} can be estimated. Because it is based on Figures 3–5, this is statistical value rather than an instantaneous measurement: It could be thought of as the observed polar cap diameter, but scaled in terms of the convection polar cap flux from the statistics of the β_{PQ} value at that α. To reduce the dependence on the α value, in addition to the $|\alpha_P - \alpha_Q| \leq 2°$ criterion, we restrict the data used in subsequent sections to passes across near the center of the polar cap with $-3° < \alpha \leq +3°$. There were 2313 such polar cap traversal of F-13 in 2001.

[32] A number of different ways of generating Figures 4 and 5, based on the same assumption, were investigated. It was found that slight variation in the absolute polar cap flux F_{PC} values (typically 5–10%) could be introduced but that the fundamental behavior in subsequent plots was not altered because changes are compensated by complementary changes to the coefficient b. The other parameters derived in this paper were found to be the same to within 1–2%.

7. Average Polar Cap Characteristics as a Function of Substorm Phase and Steady Convection Events

[33] Figure 6 and Table 1 give the mean values (and the standard errors in those means) of the various parameters for the data set of 2313 F-13 passes in 2001 across the center of the polar cap with $-3° < \alpha \leq +3°$ and with $|\alpha_P - \alpha_Q| \leq 2°$. Figure 6 shows the classifications of the substorm cycle (in order classes 1,2,3,4,5,7,1) followed by a steady convection event (SCE, in order classes 1,2,3,6,6,6,6,6,7,1: note that five consecutive means for class 6 are shown in the SCE to

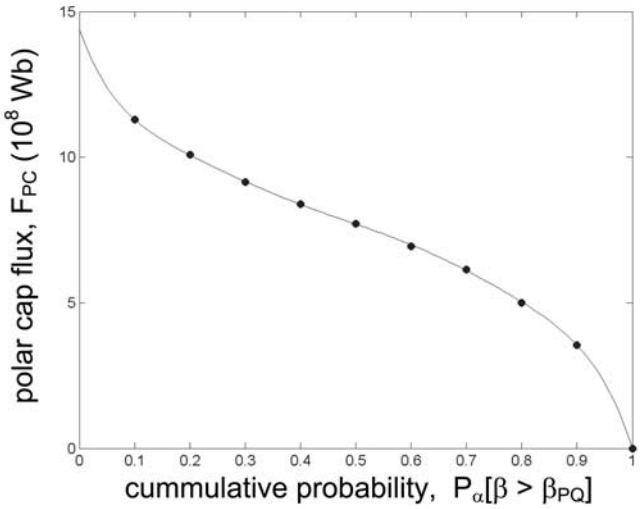

Figure 5. The solid points are the magnetic flux threading the statistical convection polar caps delineated by the solid lines in Figure 4, $F_{PC} = B_i \int_\alpha \beta_{PQ} r^2 d\alpha$, where r is the geocentric height of the satellite and B_i is the ionospheric magnetic flux density (taken to be constant at 5×10^{-5} T) as a function of the $P[\beta > \beta_{PQ}]$ threshold. The line is a 5th-order polynomial fit to the solid points. This curve is used to convert the observed angular polar cap diameter β_{PQ} into a statistical polar cap flux estimate F_{PC} by evaluating the probability that the observed β_{PQ} value is exceeded at the α of the pass, $P_\alpha[\beta > \beta_{PQ}]$, and then scaling the F_{PC} value for that $P_\alpha[\beta > \beta_{PQ}]$.

exemplify the extended nature of these events). Figures 6a–6d show (from top to bottom) the mean transpolar voltage, $\langle \Phi_{PC} \rangle$, the mean estimated convection polar cap flux $\langle F_{PC} \rangle$, the mean modified interplanetary ε parameter (ε^*) and the mean AL and AU indices (during the time of the polar cap passes). The semiempirical ε^* parameter employed here is that developed by *Reiff et al.* [1981] to allow for the fact that the IMF is amplified in the magnetosheath because it is draped over the nose of the magnetosphere in the magnetosheath and aims to predict the controlling influence on magnetopause reconnection voltage (Φ_D). The analysis presented here has been repeated using the more complex formulation of *Ridley and Kihn* [2004] and the results are almost identical (see Lockwood et al., submitted manuscript, 2008). Because it quantifies the dayside reconnection voltage (as opposed to the transpolar voltage, Φ_{PC}), ε^* is more relevant to our requirements than any of a number predictors of Φ_{PC}, based on solar wind and IMF parameters [e.g., *Boyle et al.*, 1997]. On the basis of Reiff et al., we here define

$$\varepsilon^* = V_{SW} B^* \sin^4(\theta/2) / \langle V_{SW} \rangle, \quad (6)$$

where $B^* = fB$ or $B^* = 60$ nT, whichever is the smaller. We here use $f = 7$, the value found empirically by Reiff et al. We allow for the effect of solar wind speed with the normalized factor $V_{SW}/\langle V_{SW} \rangle$ because this formulation readily allows us to study the effect on the fitted weighting factor (a), of setting this term to unity. In fact, we find that doing this (thereby removing the dependence on V_{SW}) has almost no effect on the correlation coefficient, nor on the value of a derived (but the correlation significance is actually increased because the number of fit parameters used is reduced). We include the V_{SW} term, as in equation (6), only because it makes the results presented here more directly comparable with that of Reiff et al. and other authors.

[34] To reduce any scatter due to uncertainties in the IMF monitor-to-ionosphere propagation delay, passes for which changing this lag by its estimated error causes a change in ε^* of more than 1% are omitted. This further reduces the total number of passes to 1515. Table 1 gives the numbers of samples in each class. Sample numbers are high, the lowest being 85 for prepeak expansion phases, the highest 608 for quiet intervals. It can be seen that the IMF ε^* is greatly enhanced over the quiet time mean during both substorms and SCEs. In substorms, the largest mean ε^* values are seen in the growth phases and values slowly decline thereafter, reflecting a growing probability of the IMF returning northward. Even in the recovery phases the mean value of ε^* remains quite high because many recovery phases occur despite a continuing southward IMF. The ε^* value for class 7 is low, indicating substorm and SCE activity usually ceases because the IMF had sometime previously returned northward. Note that there is a very slight decrease in ε^* between the growth and the expansion phase, but not as large as would be seen if substorm onset were routinely triggered by northward turnings of the IMF, as has been suggested (see, e.g., discussion of *Milan et al.* [2008]). The mean ε^* prevailing during SCEs is significantly greater than that during substorms. Figure 6 implies

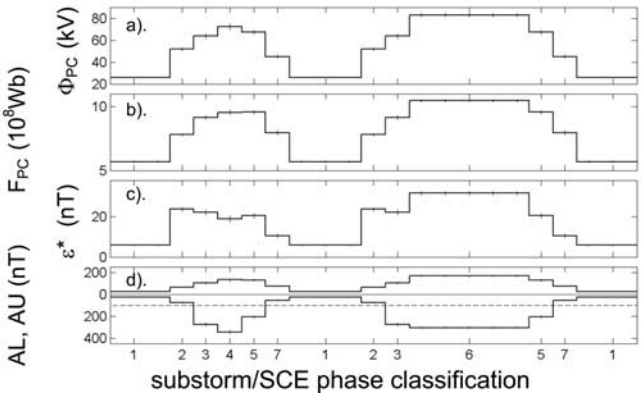

Figure 6. Means of values for all individual satellite passes meeting the criteria $|\alpha_P - \alpha_Q| \leq 2^\circ$ and $-3^\circ < \alpha \leq +3^\circ$: (a) transpolar voltage $\langle \Phi_{PC} \rangle$, (b) estimated convection polar cap flux $\langle F_{PC} \rangle$, (c) the modified solar wind/IMF ε parameter $\varepsilon^* = V_{SW} B^* \sin^4(\theta/2) / \langle V_{SW} \rangle$ (where $B^* = 7B$ or $B^* = 60$ nT, whichever is the smaller), and (d) the AL and AU indices during the pass. These are averaged over the substorm phase classifications: 1 = quiet, 2 = growth phase, 3 = prepeak expansion phase, 4 = postpeak expansion phase, 5 = recovery phase, and 7 = quiet (AL > −100 nT), but within 1 hour of the end of a recovery phase. If the expansion is followed by a steady convection event, it is classified as 6. Vertical bars give plus and minus 1 SE in the mean.

Table 1. Mean Values, Standard Errors in the Means and Best Fit Coefficients (for $n = 2$) for Fits of $\Phi_{fit} = a\varepsilon^* + bF_{PC}{}^n + \Phi_V$ Against Φ_{PC} for the Subset of 2313 Dawn-Dusk F-13 Passes During 2001 Across the Center of the Polar Cap With $|\alpha_P - \alpha_Q| \leq 2°$ and $-3° < \alpha \leq +3°$[a]

	1	2	3	4	5	6	7
Classification	Quiet	Growth	Prepeak Expansion	Postpeak Expansion	Recovery	SCE	Quiet, Post Recovery
$\langle\Phi_{PC}\rangle$ (kV)	25.96	51.58	63.55	72.08	67.31	82.88	44.89
SE δ_Φ (kV)	0.43	1.49	2.32	3.41	2.07	1.80	1.83
$\langle F_{PC}\rangle$ (10^8 Wb)	5.30	7.30	8.55	8.93	8.94	9.79	7.43
SE δ_F (10^8 Wb)	0.07	0.12	0.15	0.18	0.13	0.10	0.18
ε^* (nT)	5.40	23.25	23.85	20.19	21.62	33.90	10.54
SE δ_ε (nT)	0.28	0.90	1.49	1.79	1.35	1.03	1.21
a (kV nT^{-1})[b]	0.43	0.87	0.67	0.77	0.46	0.31	0.65
b (kV [10^8 Wb]$^{-2}$)[b]	0.11	0.14	0.30	0.49	0.46	0.62	0.12
Φ_V (kV)[b]	20.03	24.30	26.09	17.91	21.00	12.50	31.36
a/b (10^{16} Wb^2 nT^{-1})[b]	3.98	6.31	2.24	1.58	1.00	0.50	5.62
$P[a > 0] = S[a = 0]$	0.97	1.00	0.78	0.75	0.60	0.27	0.93
$P[b > 0] = S[b = 0]$	0.61	0.19	0.61	0.86	0.96	1.00	0.17
Number of passes, N	607	169	122	85	175	264	93
Peak correlation with Φ_{fit}, r[b]	0.40	0.70	0.64	0.76	0.73	0.72	0.51
Correlation with IMF, r_{ε^*}	0.35	0.68	0.57	0.62	0.60	0.45	0.45
$\langle(\Phi_{PC} - \Phi_{fit})^2\rangle^{1/2}$ (kV)[b]	26.13	22.50	31.98	30.94	26.39	31.00	30.51

[a] ε_Φ is the standard error in the mean transpolar voltage $\langle\Phi_{PC}\rangle$; ε_F is the standard error in the mean convection polar cap flux $\langle F_{PC}\rangle$; and ε_B is the standard error in the mean value of the IMF ε^*) The number of passes N, the peak correlation coefficients (r between Φ_{PC} and Φ_{fit} and $r_\varepsilon{}^*$ between Φ_{PC} and ε^*), and the RMS difference between Φ_{fit} and Φ_{PC} are also given. Values are given for the seven substorm or steady convection event (SCE) classifications defined in the text.

[b] This is for $n = 2$.

an upward step in ε^* around the time of the first substorm expansion could be part of the reason why an SCE forms.

[35] The mean convection polar cap flux $\langle F_{PC}\rangle$ is found to be very slightly greater in the recovery phase than in the expansion phase and starts to decrease only after the end of the recovery phase (here defined as when AL returns to above the −100 nT threshold, as seen in the Figure 6d). From equation (1) this implies that nightside voltage (the rate of closure of open flux) only dominates over the dayside voltage after the substorm, as detected by magnetometers, has died away. This result is consistent with the study by *Milan et al.* [2007]. They used the radar mapped potential technique with FUV auroral images to study flow across the open-closed boundary (in its own rest frame) for 9 intervals containing 22 substorm events. They found that shortly after onset the inferred Φ_N was surprisingly well matched to Φ_D for this survey of 22 case studies. Thus they also deduced that at the substorm onset the nightside reconnection increased to halt the polar cap growth, but that destruction of open flux did not commence until later. We here find the same conclusion from a statistical survey of 1 year's data.

[36] Figure 6b shows that the mean polar flux $\langle F_{PC}\rangle$ is greater in SCEs than the peak reached in substorms. The mean transpolar voltage $\langle\Phi_{PC}\rangle$ peaks in the expansion phase, after the minimum AL, but remains high in phases 5

Table 2. Same as Table 1 for Quiet and Disturbed AL Index Groupings of Classifications

	AL > −100 nT	AL ≤ −100 nT		
	1 and 2	3, 4, 5, and 6	6	3, 4, and 5
Classification	Quiet or Growth	All Disturbed AL	Steady Convection Event	Substorm Expansion and Recovery
$\langle\Phi_{PC}\rangle$ (kV)	31.97	67.13	82.88	73.79
SE δ_Φ (kV)	0.60	1.98	1.80	1.16
$\langle F_{PC}\rangle$ (10^8 Wb)	5.77	9.23	9.79	8.82
SE δ_F (10^8 Wb)	0.07	0.07	0.10	0.09
ε^* (nT)	9.42	27.18	33.90	10.54
SE δ_ε (nT)	0.38	0.70	1.03	1.21
a (kV nT^{-1})[a]	0.86	0.46	0.31	0.52
b (kV [10^8 Wb]$^{-2}$)[a]	0.14	0.52	0.62	0.58
Φ_V (kV)[a]	18.54	16.97	12.55	0.00
a/b (10^{16} Wb^2 nT^{-1})[a]	6.31	0.89	0.50	1.41
$P[a > 0] = S[a = 0]$	1.00	0.81	0.27	0.90
$P[b > 0] = S[b = 0]$	0.48	1.00	1.00	0.99
Number of passes, N	776	646	264	382
Peak correlation with Φ_{fit}, r[a]	0.73	0.73	0.72	0.70
Correlation with IMF, r_{ε^*}	0.71	0.56	0.45	0.57
$\langle(\Phi_{PC} - \Phi_{fit})^2\rangle^{1/2}$ (kV)[a]	17.01	29.34	31.00	29.81

[a] This is for $n = 2$.

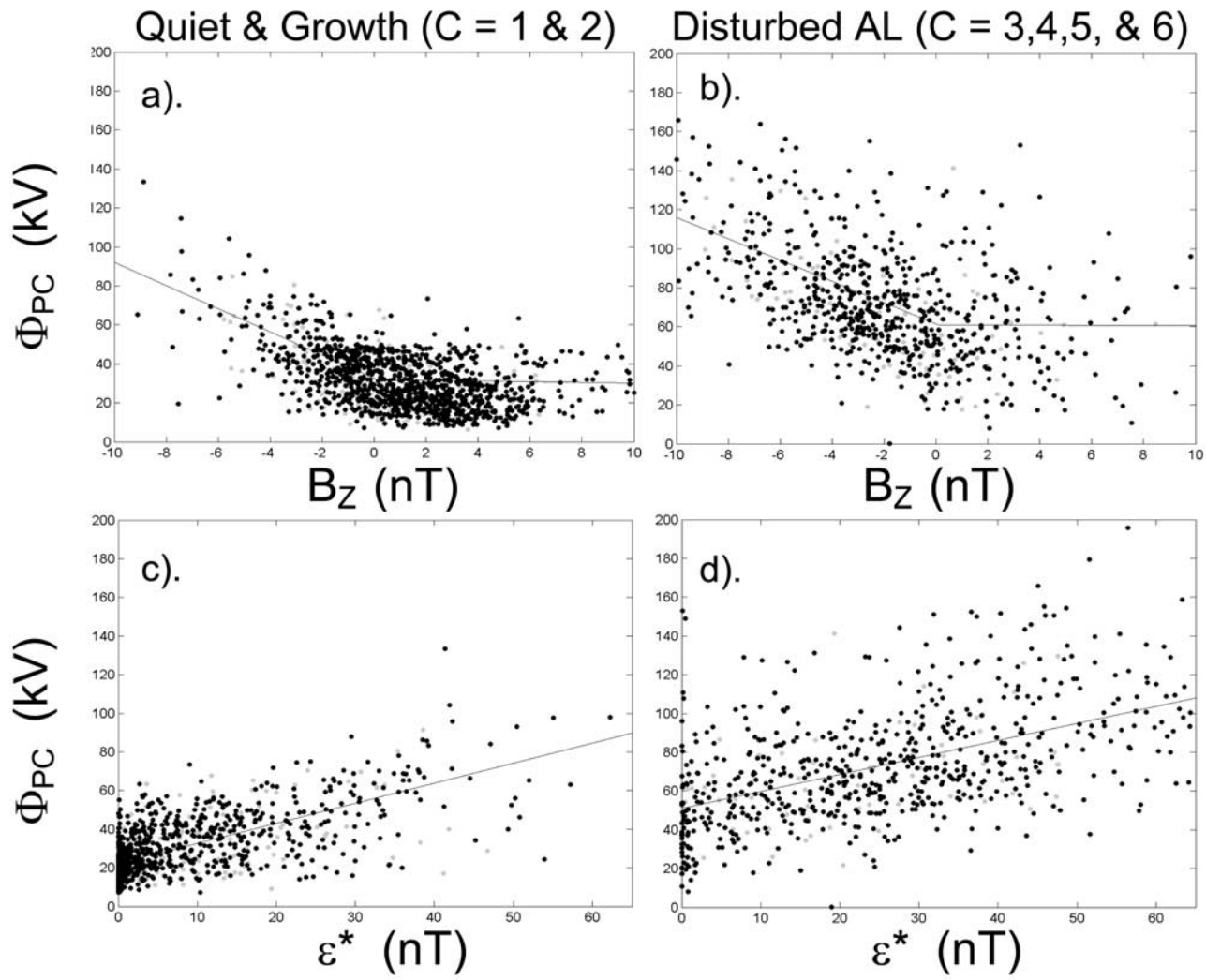

Figure 7. Scatterplots of transpolar voltage Φ_{PC} as a function of (top) IMF B_Z component in the GSM frame and (bottom) ε^* for (left) quiet/growth phase samples (classes 1 and 2) and (right) samples with large excursions of AL (AL < 100 nT), i.e., substorm expansion and recovery phases and steady convection events (classes 3, 4, 5, and 6). The data set used are the 2313 F-13 passes in 2001 across the center of the polar cap, with $-3^\circ < \alpha \leq +3^\circ$ and with $|\alpha_P - \alpha_Q| \leq 2^\circ$. Light gray points are passes for which the uncertainty in ε^*, allowing the propagation lag uncertainty from the solar wind monitor spacecraft to the polar ionosphere, exceeds 1% nT. Black points are for points with uncertainty below this threshold. The lines are linear fits to all the black points in each set for $B_z > 0$ and $B_z \leq 0$.

and 7 (i.e., in recovery and for at least one hour subsequently). As for $\langle F_{PC} \rangle$, $\langle \Phi_{PC} \rangle$ is higher in SCEs than the peak seen during the substorm cycle.

8. Analysis in Terms of the Expanding-Contracting Polar Cap Model

[37] In order to illustrate the principles of the analysis, we make use of three groupings of classes: quiet AL periods (classes 1 and 2), all disturbed AL periods (classes 3,4,5 and 6) and, for comparison with SCEs (class 6), substorm disturbed AL periods (classes 3,4 and 5). The numbers of passes and mean values, as given for each class individually, are given in Table 2. Figures 7a and 7b show scatterplots of Φ_{PC} as a function of IMF B_z for quiet AL conditions (classes 1 and 2) and for disturbed AL (classes 3,4,5 and 6). The black points are where the uncertainty in the estimated propagation lag gives a change in ε^* of less than 1%, the gray points are where this threshold is exceeded. A range of thresholds for this uncertainty was tried and it was found that the general patterns and results were not altered. The black lines are linear fits to all the black points in each set for $B_z > 0$ and $B_z \leq 0$, constrained to have the same value at $B_z = 0$. It can be seen from comparison of Figures 7a and 7b that disturbed AL case shows the same form of "half wave rectified" dependence of IMF B_z but that mean values are higher and there is considerably greater scatter for the disturbed AL periods.

[38] Several studies report a dependence of transpolar voltage on the dawn-to-dusk interplanetary motional electric field using a form such as $V_{sw}B\sin^4(\theta/2)$ [e.g., *Eriksson et al.*, 2001]. In addition several statistical fits have introduced

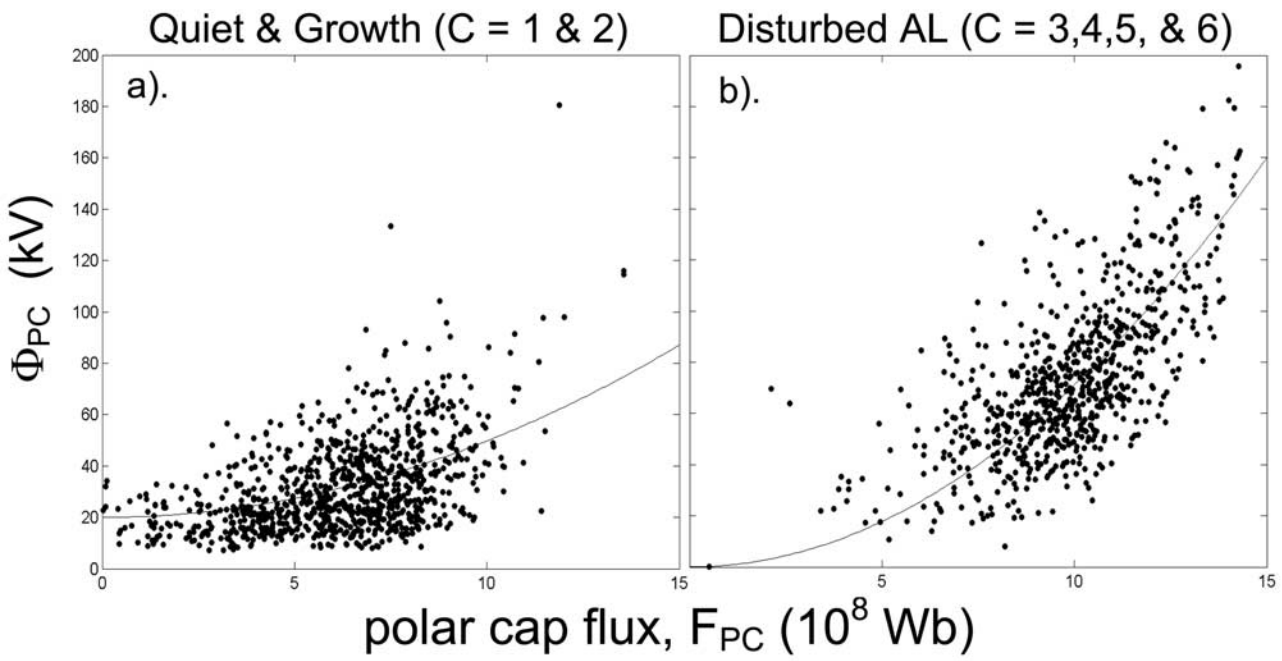

Figure 8. Scatterplots of transpolar voltage Φ_{PC} as a function of the estimated convection polar cap flux F_{PC} for (a) samples in classes 1 and 2 and (b) samples in classes 3, 4, 5, and 6. The data set used is the same as in Figure 7.

an additive term dependent on V_{sw} [e.g., *Boyle et al.*, 1997; *Ridley*, 2005]. In the study presented here, none of the correlations were improved by the introduction of either a multiplicative or an additional term dependent on V_{SW}. Figures 7c and 7d show the corresponding scatterplots as a function of ε^*. The correlation coefficients between Φ_{PC} and ε^* (r^*_ε) are given in Table 2.

[39] Figure 7 shows that an additional factor, other than the IMF or interplanetary electric field, is influencing Φ_{PC} during disturbed AL. The ECPC model predicts that this factor is the field line closure reconnection voltage in the cross-tail current sheet and equation (3) quantifies this as bF^n_{PC}. Figure 8 plots Φ_{PC} as a function of F_{PC} for the same two data sets as Figure 7. The solid lines show the best fit lines of the form $bF^n_{PC} + c$. In the quiet AL case, the best fit value of n is near 1.5, for the disturbed it is near 2.5. However in both cases the peak of the variation of correlation coefficient with n is very flat and we here use the best fit for the two data sets combined which is $n = 2$. Note that the coefficient b is considerably smaller for the quiet AL case. Hence Φ_{PC} for the disturbed AL conditions is showing much greater dependence on the polar cap flux, F_{PC}.

[40] Figure 9 shows the best fits to the observed Φ_{PC} data points, Φ_{fit}, using equation (4) and for the same two data sets as Figures 7 and 8. Fits are generated using the Nelder-Mead simplex (direct search) method [*Nelder and Mead*, 1965; *Lagarias et al.*, 1998] to minimize the RMS difference between Φ_{PC} and Φ_{fit}. The exponent n used is 2, as in Figure 8. The straight line is the ideal agreement $\Phi_{PC} = \Phi_{fit}$. The degree of scatter is now similar in the two cases and the linearity is preserved throughout the range of Φ_{PC}. The best fit values of a, b and Φ_V are given in Table 2. The correlation coefficient between Φ_{PC} and Φ_{fit} (r) exceeds 0.7 in all cases and exceeds that between Φ_{PC} and ε^* (r^*_ε) for all the disturbed AL cases. Using the Fisher-Z test, the differences between r and r^*_ε are significant at almost the 100% level (Lockwood et al., submitted manuscript, 2008). In order to analyze the relative effect of the first two terms in equation (4) (due to magnetopause and tail reconnection) the ratio of the two coefficients (a/b) was fixed at a range of preset values, the best fit to Φ_{PC} then generated by iterating a (and hence for the fixed a/b value, b also) and Φ_V and the correlation coefficient, r, between Φ_{PC} and Φ_{fit} evaluated for that (a/b) value. Figures 10a and 10b show the variation of correlation coefficient r with $\log_{10}(a/b)$. In each case, the peak correlation (for the best fit given in Figure 9) is marked with a vertical dashed line. It can be seen that the peak r is not that much greater than obtained from neighboring (a/b) values. To analyze the uncertainty in the derived best (a/b), and hence the ratio of the reconnection terms in equation (4), Figures 10c and 10d evaluate the statistical significance S of the difference between the peak correlation and values at other (a/b) values. This is done using the Fisher-Z statistic, using the procedure given by *Lockwood* [2002b]. The horizontal dashed lines in Figures 10c and 10d are for $S = 0$, 1 and 0.9 and the points where $S = 0.9$ are also marked with vertical dashed lines, which are also extended into Figures 10a and 10b. These points are thus where the correlation coefficient has fallen below the peak value to a level that is statistically significant at the 90% level. Note that in the case of the quiet AL conditions, this level is still not reached at the largest $\log_{10}(a/b)$ shown (= 2.5, i.e., $a = 316b$). In fact, for $b = 0$ ($a/b = \infty$) we find an S value of $S[b = 0] = 0.48$ (also given in Table 2) and hence we can say that the detection of a nightside voltage, dependent on F_{PC}, is only significant at the 48% level for these quiet AL conditions. On the other hand, for these quiet conditions, the correlation for $a = 0$ ($a/b = 0$) gives an S value $S[a = 0]$ of

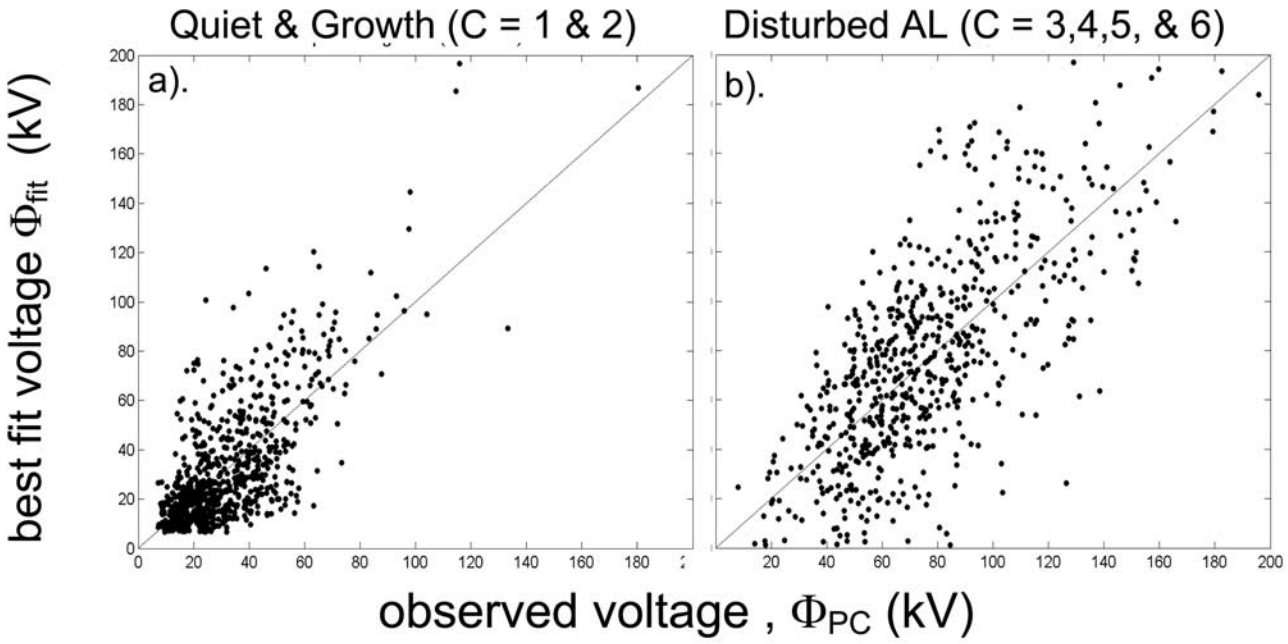

Figure 9. Scatterplots of the best least squares fit $\Phi_{fit} = a\varepsilon^* + bF_{PC}{}^n + \Phi_V$ against Φ_{PC} for (a) samples in classes 1 and 2 and (b) samples in classes 3, 4, 5, and 6. The data set is the same as used in Figures 7 and 8. The diagonal lines are $\Phi_{fit} = \Phi_{PC}$. The best fit a, b, and Φ_V are given in Table 2.

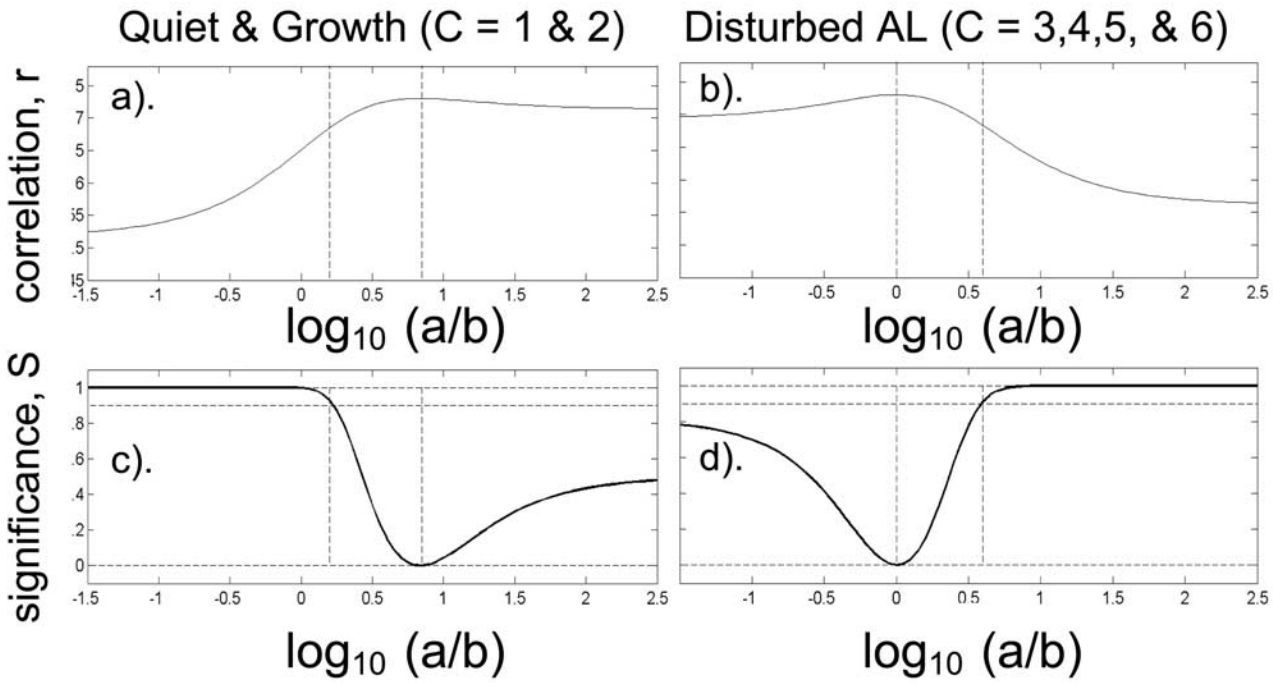

Figure 10. Correlograms for samples in (left) classes 1 and 2 and (right) classes 3, 4, 5, and 6 for the same data set as in Figures 6–8. In each case, Figures 10a and 10b show the correlation coefficient between $\Phi_{fit} = \{a\varepsilon^* + bF_{PC} + \Phi_V\}$ and Φ_{PC} as a function of the $\log_{10}(a/b)$. The peak is marked with a vertical dashed line (scatterplots for this a/b are given in Figure 9). Figures 10c and 10d show the significance S of the difference in the correlations at the peak and at other values of (a/b), computed using the Fisher-Z test. The horizontal lines are drawn for S of 1, 0.9, and 0. The vertical dashed lines either side of the peak mark the (a/b) where the correlation is lower than the peak value by a difference that is significant at the 90% level (note that the upper of these two limits is off scale in the left-hand plot, as is the lower limit in the right-hand plots). The best fit parameters are given in Table 2.

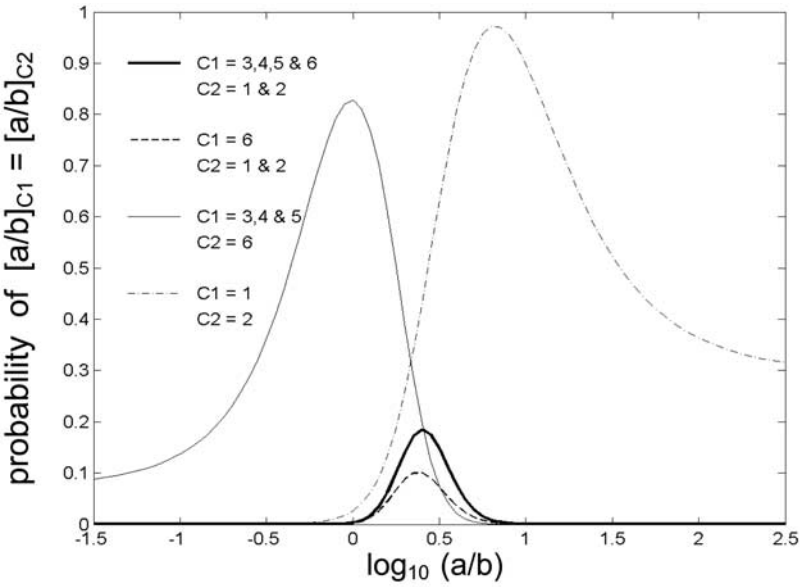

Figure 11. Analysis of the probability that the ratio of the coefficients (a/b) is the same for different pairs of classifications. Thick solid line: disturbed conditions (i.e., classes 3, 4, 5, and 6) compared with quiet times and growth phases (classes 1 and 2). Dashed line: steady convection events (class 6) against quiet times and growth phases (classes 1 and 2). Dash-dotted line: quiet time (class 1) against substorm growth phases (class 2). Thin solid line: steady convection events (class 6) against substorm disturbed times (classes 3, 4, and 5).

unity (to within 2 decimal places) and so there is nigh-certain detection (> 99%) in these quiet data of the IMF influence quantified by ε^*. Note that Figure 8a appears to show a clear dependence on F_{PC} under quiet conditions, but the scatter and the intercorrelation between F_{PC} and ε^* means that statistically it is only significant at the 48% level.

[41] Conversely for the disturbed AL data (classes 3,4,5 and 6), we find $S[b = 0] = 1.00$ and $S[a = 0] = 0.81$. This means that that the detection of the influence of the nightside voltage, dependent on the polar cap flux F_{PC}, is >99% certain and that the additional influence of a dayside voltage, proportional to ε^*, is 81% certain.

[42] Thus these plots confirm that the transpolar voltage is governed by the ECPC model with two contributions detected: one depends on the IMF strength and orientation, ε^*, the other on the polar cap flux squared, F_{PC}^2. However, the strength of these contributions change during the substorm cycle. Both are detected during disturbed times, but during quiet times and substorm growth phases, the tail reconnection term giving the dependence on F_{PC}^2, is only detected at the 48% significance level. During steady convection events, the effect of F_{PC}^2 is detected at essentially the 100% level, but the effect of the IMF forcing is found at only the 27% level.

[43] Table 2 shows that the coefficient a is greater in quiet/growth intervals than in disturbed AL times by a factor of about 2. This implies that the magnetopause reconnection voltage depends on the IMF (and possibly other solar wind parameters) but does also depend on the magnetospheric substorm phase, as predicted by the theories of transpolar voltage saturation (see Lockwood et al., submitted manuscript, 2008). On the other hand, Table 2 shows that the best estimate of b in quiet/growth phases is about one quarter of the value during disturbed AL times (note that, from the above, there is a 48% chance that b is actually zero during quiet/growth intervals). Thus the ratio (a/b) is lower by a factor of about 8 during disturbed AL than in quiet/growth intervals. For SCEs, (a/b) is an order of magnitude smaller than for quiet/growth intervals. The reasons for this are discussed in section 9, but in the remainder of this section we investigate if (a/b) could, in fact, be the same in quiet/growth and disturbed AL intervals.

[44] To achieve this, we use the probability that the correlation is less than the peak for a given class C (S_C, as given in Figures 10c and 10d). Thus the probability that both class C1 and class C2 could actually have the same value of (a/b), $P_{[C1,C2]}$, is given by

$$P_{[C1,C2]} = (1 - S_{C1}) \times (1 - S_{C2}) \quad (7)$$

[45] Figure 11 shows the probabilities $P_{[C1,C2]}$, computed using equation (7), for various combinations of classifications, as a function of $\log_{10}(a/b)$. The thin solid line compares steady convection events (C2 of 6) with substorm disturbed AL (C1 is 3, 4, or 5). It can be seen that the probability that both have value of 1×10^{16} Wb^2 nT^{-2} is 0.83. Thus SCEs and substorms are similar in their (a/b) behavior, but not identical. The dash-dotted line compares classes 1 and 2 (i.e., quiet against growth) and the possibility that both have (a/b) near 6×10^{16} Wb^2 nT^{-2} has a probability of 0.98. Thus growth phases and quiet intervals appear to be the same in their (a/b) behavior and only differ because the ε^* value is higher during growth phases. The thick solid line gives the probability that (a/b) is the same for of quiet/growth phases (C2 is class 1 or 2) and disturbed AL phases (C1 is class 3,4,5 or 6). It can be seen that if they

were the same, the most likely common value is near (a/b) = 2.5×10^{16} Wb^2 nT^{-2} (i.e., $\log_{10}(a/b) = 0.4$) but the probability of this is only 0.18. Thus the difference in (a/b) values for quiet and disturbed conditions is significant at the 82% level. SCEs and quiet/growth periods are even more clearly distinct, the dashed line showing the probability of them sharing the same (a/b) is only 8%.

9. Analysis of Classifications Separately

[46] Section 7 shows significant differences between intervals of quiet/growth and disturbed AL. The analysis presented for the grouped classifications presented in Table 2 was repeated for each classification individually and the results are presented in the lower half of Table 1. Peak correlations near 0.7 were obtained for all phases except the quiet ones (1 and 7): these are consistent with the values obtained for the groupings of classes (and hence larger sample sizes) discussed in Table 2.

[47] Magnetopause reconnection voltage could not be detected with 100% certainty at all phases, the probability of it being present being 97%, >99% and 93% for quiet, growth and postrecovery phases, respectively, but only 78%, 75% and 60% for the two substorm expansion phase classifications and the recovery phases. For SCEs it is as low as 27%. The probability of polar cap flux influence grows during substorm cycles and is 96% for recovery phases and >99% for steady convection events. Before then it rises from 19% for growth phases to 61% for prepeak expansion phases, to 86% for postpeak expansion. Immediately after the recovery phase the detection of the F_{PC}^2 signal returns to being as uncertain as it was during the growth phase and the (a/b) ratio has returned to a value typical of quiet/growth. However, Figure 6 shows that the magnetosphere has not yet returned to its presubstorm state: the average value of ε^* is marginally higher than during quiet times (reflecting the persistence of the IMF data series) but the mean transpolar voltage Φ_{PC} is significantly higher than during quiet intervals and the polar cap flux F_{PC} is also considerably enhanced, actually exceeding its average value during growth phase.

10. Discussion

[48] *Bristow et al.* [2004] studied the transpolar voltage from SuperDARN radar observations for the same year as studied here, i.e., 2001. They note that there is considerable scatter in comparisons between transpolar voltage and the best fit values Φ'_{fit}, derived from the interplanetary electric field only (i.e., for $b = 0$), even although their survey was restricted to stable IMF conditions: they report the average uncertainty $|\Phi_{PC} - \Phi'_{fit}|$ is 20 kV, and the fractional uncertainty ($|\Phi_{PC} - \Phi'_{fit}|/\Phi_{PC}$) typically varied between 25% and 50%. The survey presented here is not restricted to steady IMF conditions and shows that the large scatter in the data can be reduced (and $r > r^*_\varepsilon$) if, in addition to the interplanetary electric field, the convection polar cap magnetic flux F_{PC} is considered along with the phase of the solar cycle and the AL value.

[49] The Expanding-Contracting Polar Cap (ECPC) model of ionospheric convection was developed to give an understanding of ionospheric flow in nonsteady conditions. It predicts that the instantaneous transpolar voltage will be a combination of the voltage along the magnetopause X line and that along the X line in the cross-tail current sheet at which open field lines are being closed, with a small viscous-like contribution [*Lockwood*, 1991; *Lockwood and Cowley*, 1992; *Milan*, 2004]. The ECPC model also predicts that the ratio of these two voltage contributions is expected to vary during the substorm cycle with the magnetopause voltage dominating during substorm growth phases and the tail X line voltage expected to dominate during the later stages of the substorm cycle. Many of these characteristics have all been revealed in the study presented here, but with some notable differences that we discuss in this section.

[50] The dominant influence on the transpolar voltage during disturbed AL intervals is the polar cap flux F_{PC}, an influence which grows during prior periods of southward IMF. The intervals yielding large b (and hence a strong and significant dependence on F_{PC}) are those for which the Near-Earth Neutral Line (NENL) is expected to be close to the Earth. Once the NENL has reconnected all the closed flux and pinched off the plasmoid it takes over from the far X line in setting Φ_N. While it is close to the Earth, the magnetic shear across the NENL depends on F_{PC} but this dependence is expected to weaken as the NENL retreats down the tail. The value of b is a bit lower in recovery phases than in expansion phases and SCEs, but the major decline in b does not occur until after the recovery phase (the recovery phase being defined by AL and hence the substorm current wedge/auroral electrojet current system).

[51] In order to understand the cycle better, Figure 12 analyzes the contributions to the mean transpolar voltages using the same format as Figure 6. Figure 12a shows the observed mean voltage for a given pass classification, Φ_{PC}, as a histogram and compares it to the sum of the best fit components (namely $\Phi_D = a\ \varepsilon^*$; $\Phi_N = bF_{PC}^n$ and Φ_V, see equation (4)), shown as dots. It can be seen that the fit accounts for the total observed mean voltages very well. Figure 12b compares the means $\langle\Phi_D\rangle = a\ \langle\varepsilon^*\rangle$ (thin solid line) and $\langle\Phi_N\rangle = b\ \langle F_{PC}\rangle^n$ (thick solid line) for the best fit a, b and n for each pass classification. It can be seen that $\langle\Phi_N\rangle$ exceeds $\langle\Phi_D\rangle$ for all classifications except 1 and 7 (for which they are almost equal) and 2, for which $\langle\Phi_N\rangle = 7.36$ kV and $\langle\Phi_D\rangle = 20.25$ kV, respectively, a difference of $\langle\Phi_D\rangle - \langle\Phi_N\rangle = 12.89$ kV. Figure 6 shows that, on average, the polar cap flux $\langle F_{PC}\rangle$ rises during growth phases from 5.30×10^8 Wb during quiet periods (class 1) to 8.55×10^8 Wb during early expansion phases (class 3). This is an average rise of 3.25×10^8 Wb, which at 12.89 kV would take $\Delta F_{PC}/(\Phi_D - \Phi_N) = 7.00$ hours. This is considerably longer than the duration of most growth phase intervals in this study.

[52] Furthermore, the mean dayside and nightside voltages detected during intervals of class 7 are $\langle\Phi_D\rangle = 6.82$ kV and $\langle\Phi_N\rangle = 6.36$ kV. This would imply that the polar cap was almost in steady state (in fact growing at a tiny rate) during intervals of class 7. However, Figure 6 shows that, in fact, the polar cap flux falls during such intervals. Thus at least some of the large Φ_V (31.36 kV) detected during these intervals must actually be nightside reconnection voltage, but which is not dependent on the polar cap flux. We propose that this voltage is not detected as $\Phi_N = b\ F_{PC}^n$ because the near-Earth neutral line has retreated sufficiently far down

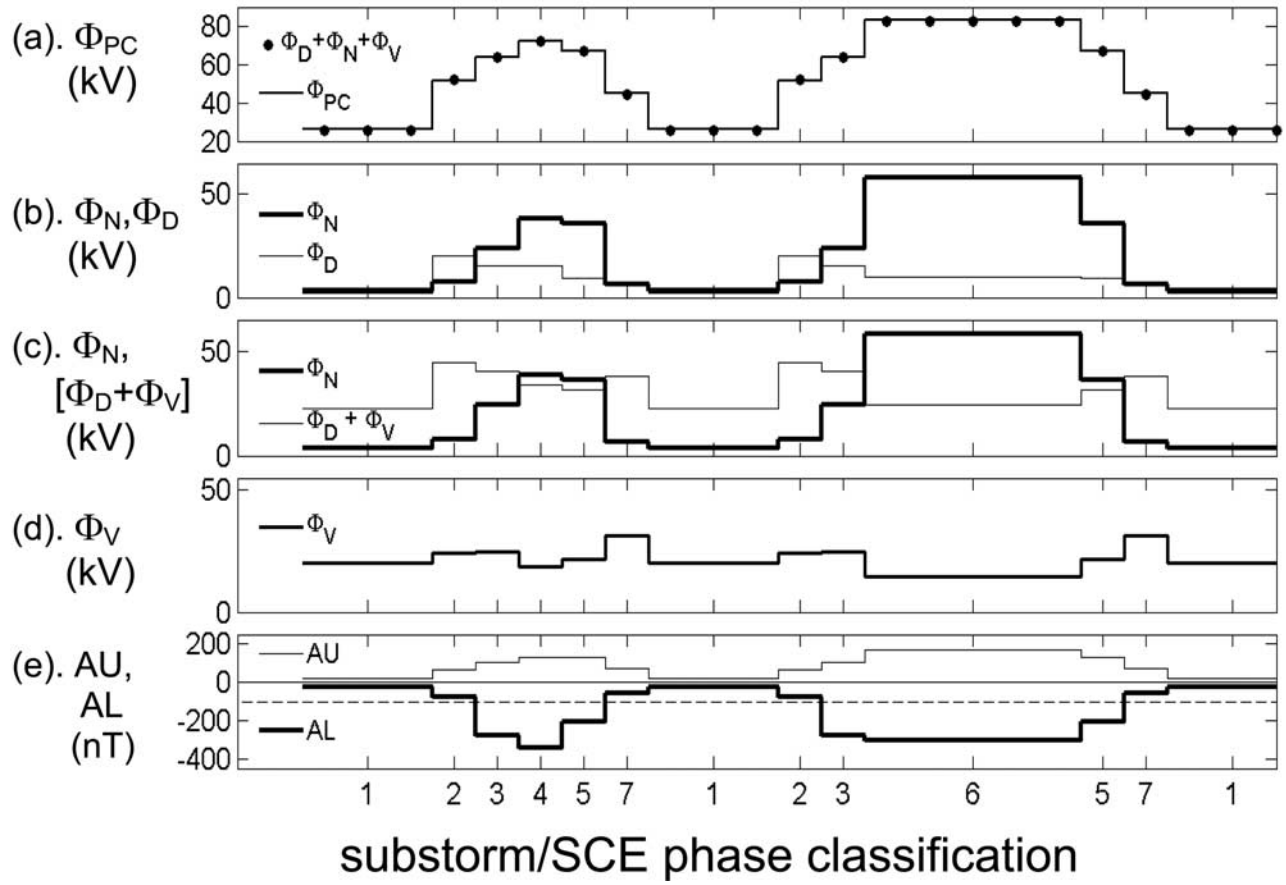

Figure 12. The derived breakdown of mean voltages for different classes. From top to bottom: (a) the observed total $\langle\Phi_{PC}\rangle$ (line) compared to $\langle\Phi_D\rangle + \langle\Phi_N\rangle + \langle\Phi_V\rangle$ (dots), where $\langle\Phi_D\rangle = \langle a\rangle\langle\varepsilon^*\rangle$ and $\langle\Phi_N\rangle = \langle b\rangle\langle b\rangle\langle F_{PC}\rangle^2$; (b) $\langle\Phi_D\rangle$ (thin line) compared to $\langle\Phi_N\rangle$ (thick line); (c) $\langle\Phi_D+\Phi_V\rangle$ (thin line) compared to $\langle\Phi_N\rangle$ (thick line); (d) $\langle\Phi_V\rangle$; and (e) $\langle$AU$\rangle$ (thin line) and $\langle$AL$\rangle$ (thick line).

the tail that the magnetic shear across it is set by the interplanetary static pressure and is therefore largely independent of F_{PC}.

[53] Panel 4 shows the fitted "viscous-like" (non reconnection) voltage Φ_V. In fact, this voltage can have four possible origins: (1) dayside reconnection generating open field lines that is not well quantified by the $a\varepsilon^*$ factor [e.g., *Phan et al.*, 2005]; (2) nightside reconnection that, as discussed above, closes open field lines but is not well quantified by the bF_{PC}^n factor, which, as pointed out by *Lockwood and Cowley* [1992] and *Fox et al.* [1994], can mimic viscous-like interaction flow patterns; (3) genuinely viscous-like interaction moving closed field lines into the geomagnetic tail; and (4) nightside reconnection pinching off closed field lines that have been dragged into the tail by viscous-like interaction [see, for example, *Lockwood et al.*, 1988].

[54] One notable feature of Figure 12d is that the inferred Φ_V is not independent of substorm phase and that, although it often is in the range 20–25 kV, it falls to 12.5 kV in SCEs. If this viscous voltage is assumed to be independent of substorm phase, SCEs set an upper limit of the true viscous voltage which is consistent with the voltage simulated by *Sonnerup et al.* [2001] using MHD models in the absence of any IMF (and hence magnetopause reconnection) and with the voltage observed by *Wygant et al.* [1983] from satellite data after prolonged intervals of northward IMF. In fact, several previous studies have reported more restrictive limits to this viscous-like voltage: *Milan* [2004] deduced an upper limit of 10 kV from studies of the rate of expansion and *Hapgood and Lockwood* [1993] and *Mozer et al.* [1994] deduced even smaller values from observations at the magnetospheric flanks (with proper allowance for boundary motion effects on the measurement). Recently, K. A. Drake et al. (The electrostatic potential drop across the ionosphere signature of the low latitude boundary layer, submitted to *Journal of Geophysical Research*, 2008) found a mean value near 10 kV for the 06-18 MLT meridian by studying the mean voltage across the region of LLBL precipitation.

[55] If we adopt a value of 10 kV of the derived Φ_V being due to a genuine viscous-like interaction acting on closed field lines, the remainder is due to either Φ_D or Φ_N which has not been adequately quantified by the fit procedure employed here. We here explore two possible implications of this idea. Firstly, a real viscous voltage of 10 kV would mean that 14.30 kV of the inferred Φ_V during growth phases could be due to magnetopause reconnection and if added to the detected Φ_D, the mean dayside voltage in growth phases would then exceed the mean nightside voltage by 27.10 kV and the average growth phase rise of 3.25×10^8 Wb, described above, would take 3.3 hours, which is more

typical of an integrated growth phase duration. Secondly, his could also mean that 21.36 kV of the apparently viscous voltage of 31.36 kV seen immediately after a substorm recovery phase was due to nightside reconnection. Adding this to the detected $(\Phi_N - \Phi_D) = -0.46$ kV for this phase gives an excess nightside voltage of 20.90 kV. The mean polar cap flux during the recovery phase is $F_{PC} = 8.94 \times 10^8$ Wb and this must fall to the quiet time average of 5.30×10^8 Wb during the interval after the substorm/SCE cycle. At the above inferred voltage this would take $\Delta F_{PC}/(\Phi_D - \Phi_N) = 4.83$ hours. This is reasonably consistent with the decay time constant of the excess flux following a recovery phase. We conclude that using a genuine viscous-like voltage of 10 kV, and assuming the other part of the inferred Φ_V comes from, respectively, magnetopause/nightside reconnection during growth phases/expansion-recovery phases gives plausible time constants for polar cap expansion and contraction.

[56] Figure 12c compares Φ_N with the sum $(\Phi_D + \Phi_V)$ which is the total flux transfer rate across the central (convection) polar cap of both open and closed field lines. The only exception to this is immediately after recovery phases when, as discussed above, some of the inferred Φ_V appears to be due to Φ_N. It can be seen that Φ_N and $(\Phi_D + \Phi_V)$ are very similar indeed in postpeak substorm expansion and recovery phases. The rough equality of $(\Phi_D + \Phi_V)$ and Φ_N is consistent with Figure 6 in that the polar cap flux doesn't begin to decay until the end of the recovery phase. As discussed earlier, this is also consistent with the survey of 22 case studies by *Milan et al.* [2007]. There is an interesting difference with SCEs for which Φ_N is close to twice $(\Phi_D + \Phi_V)$. This would imply that SCEs are not caused by a balance between dayside and nightside voltages, rather because very large polar flux has accumulated and this can drive dominant tail reconnection for an extended interval. Figure 6 shows that the polar cap flux in SCEs, on average, is indeed larger than the peak seen during substorm cycles and, given that Φ_N is here found to depend on F_{PC}^2, this gives a considerably enhanced Φ_N. One reason why the polar cap flux might grow exceptionally large prior to steady convection events (which then drives a sustained period of high Φ_N) has been suggested by *Milan et al.* [2008] from a study of a 10-day interval containing 49 substorms. They found evidence that suggests the tail may become less unstable to reconnection if the ring current is enhanced. This being the case, a delay is expected while the ring current decays before an SCE can begin, or indeed before tail reconnection can begin to reduce the accumulated open flux in many substorms.

11. Conclusions

[57] We have studied the average characteristics of the transpolar voltage during the various phases of substorms and steady convection events. The key findings are as follows:

[58] 1. All phases of substorms/SCEs show some indication of a contribution to the transpolar voltage by both the dayside reconnection voltage Φ_D (quantified by the modified interplanetary electric field, ε^*) or Φ_N (quantified using the polar cap flux, F_{PC}). However, the probability of the detection of each varies considerably during substorm/SCE cycles.

[59] 2. Detection of the interplanetary influence via Φ_D is 97% certain during quiet intervals and >99% certain during substorm/SCE growth phases. However, it falls to 75% during substorm expansion phases and, remarkably, is only 27% in SCEs.

[60] 3. Detection of the polar cap flux influence via Φ_N is only 19% certain during growth phases, rising to 86% in expansion phases and 96% in recovery phases. During SCEs it is >99%.

[61] 4. The second surprising finding about SCEs, and one that is consistent with both points 2 and 3, is that the transpolar voltage is dominated by Φ_N. It therefore appears that SCEs occur because of the accumulation of unusually large F_{PC} (which then takes a long time to be eroded away), not because Φ_D and Φ_N attain roughly equal values. The rise in average Φ_D seen at the start of SCEs may help this build up of a large F_{PC}, but the chief reason appears to be a failure of the first expansion to destroy sufficient open flux.

[62] 5. The substorm expansion phase appears, on average, to only halt the rise in F_{PC} rather than reverse it, so, on average, polar cap fluxes remain as high (actually slightly higher) in recovery phases as they were at the end of the growth phase. The main destruction of the excess open flux appears to take place after the recovery phase in AL and to take at least 5 hours. It is expected that if this destruction is interrupted by a return to, or continued, southward IMF, a shorter duration growth phase would ensue.

[63] 6. The influence of F_{PC} on the transpolar voltage is low in postrecovery quiet intervals and in other quiet phases. This is consistent with the idea that the X line closing open flux (what had been the NENL) has migrated antisunward down the tail: as it does so the influence of F_{PC} on the magnetic shear across the X line diminishes. It is expected that Φ_{PC} and Φ_N will then depend primarily on the static pressure of the interplanetary medium. This will be addressed in a subsequent paper.

[64] 7. The residual fit voltage Φ_V is 20–25 kV in all phases. However, the changes in F_{PC} show that at least some of this is undetected dayside or nightside voltage (in the case of growth phases and postrecovery phases, respectively) and not genuine viscous-like transport of closed field lines into the tail. The required growth/shrink rates imply the true viscous-like voltage is about 10 kV. The remainder is supplied by the ability for reconnection to generate open field lines at a low background rate, even when the IMF is northward [e.g., *Phan et al.*, 2005] and the fact that the substorm cycle leaves the magnetosphere in a higher F_{PC} state, the excess being slowly removed by Φ_N which contributes to Φ_{PC} [*Lockwood and Cowley*, 1992; *Fox et al.*, 1994].

[65] 8. The reduction of the coefficient a during intervals of large F_{PC} (Tables 1 and 2) supports the concept that transpolar voltage saturation is due to magnetopause reconnection efficiency decreasing as the polar cap flux increases [see *Siscoe et al.*, 2004]. This feature is discussed further by (Lockwood et al., submitted manuscript, 2008).

[66] **Acknowledgments.** The work of M.L., A.P.R., and I.D.F. is funded by the UK Science and Technology Facilities Council, and that of

M.R.H. is by NSF grant ATM-0637791. We also thank the scientists of the SPDF and NSSDC of NASA/Goddard SFC and of the World Data Centres Kyoto and Chilton, who compiled and supplied the OMNI and AE data sets, respectively. We also wish to thank the PIs and teams of the ACE and Wind magnetometers and solar wind plasma instruments, who provided data to Omniweb.

[67] Wolfgang Baumjohann thanks Stephen Milan and another reviewer for their assistance in evaluating this paper.

References

Ahn, B. H., et al. (1992), Cross-polar cap potential difference, auroral electrojet indexes, and solar-wind parameters, *J. Geophys. Res.*, *97*(A2), 1345–1352.

Ahn, B. H., et al. (1995), Substorm changes of the electrodynamic quantities in the polar ionosphere—CDAW-9, *J. Geophys. Res.*, *100*(A12), 23,845–23,856.

Boudouridis, A., et al. (2007), Dayside reconnection enhancement resulting from a solar wind dynamic pressure increase, *J. Geophys. Res.*, *112*, A06201, doi:10.1029/2006JA012141.

Boyle, C., P. H. Reiff, and M. Hairston (1997), Empirical polar cap potentials, *J. Geophys. Res.*, *102*(A1), 111–126.

Bristow, W. A., et al. (2004), On the observed variability of the cross-polar cap potential, *J. Geophys. Res.*, *109*, A02203, doi:10.1029/2003JA010206.

Cai, X., et al. (2006), Statistical analysis of ionospheric potential patterns for isolated substorms and sawtooth events, *Ann. Geophys.*, *24*(7), 1977–1991.

Chisham, et al. (2008), Remote sensing of the spatial and temporal structure of magnetopause and magnetotail reconnection from the ionosphere, *Rev. Geophys.*, *46*, RG1004, doi:10.1029/2007RG000223.

Cowley, S. W. H. (1981), Magnetospheric and ionospheric flow and the interplanetary magnetic field, in *The Physical Basis of the Ionosphere in the Solar-Terrestrial System*, *AGARD CP-295*, pp. 4(1)–4(14), Advis. Group for Aerosp. Res. and Dev., France.

Cowley, S. W. H. (1984), Solar wind control of magnetospheric convection, in *Achievements of the Intern. Magnetospheric Study (IMS)*, *Eur. Space Agency Spec. Publ.*, ESA-SP 217, pp. 483–494, Noordwijk, Netherlands.

Cowley, S. W. H., and M. Lockwood (1992), Excitation and decay of solar-wind driven flows in the magnetosphere-ionosphere system, *Ann. Geophys.*, *10*, 103–115.

Doyle, M. A., and W. J. Burke (1983), S3-2 measurements of the polar-cap potential, *J. Geophys. Res.*, *88*(A11), 9125–9133.

Eriksson, S., L. G. Blomberg, N. Ivchenko, T. Karlsson, and G. T. Marklund (2001), Magnetospheric response to the solar wind as indicated by the cross-polar potential drop and the low-latitude asymmetric disturbance field, *Ann. Geophys.*, *19*, 649–653.

Fox, N. J., et al. (1994), EISCAT observations of unusual flows in the morning sector associated with weak substorm activity, *Ann. Geophys.*, *12*(6), 541–553.

Freeman, M. P. (2003), A unified model of the response of ionospheric convection to changes in the interplanetary magnetic field, *J. Geophys. Res.*, *108*(A1), 1024, doi:10.1029/2002JA009385.

Freeman, M. P., and D. J. Southwood (1988), The effect of magnetospheric erosion on mid-latitude and high-latitude ionospheric flows, *Planet. Space Sci.*, *36*(5), 509–522.

Freeman, M. P., et al. (1993), The interaction of a magnetic cloud with the earth: Ionospheric convection in the northern and southern hemispheres for a wide range of quasi-steady interplanetary magnetic field conditions, *J. Geophys. Res.*, *98*(A5), 7633–7655.

Grocott, A., et al. (2002), Excitation of twin-vortex flow in the nightside high-latitude ionosphere during an isolated substorm, *Ann. Geophys.*, *20*(10), 1577–1601.

Hairston, M. R., and R. A. Heelis (1995), Response time of the polar ionospheric pattern to changes in the north-south direction of the IMF, *Geophys. Res. Lett.*, *22*(5), 631–634.

Hairston, M. R., et al. (1998), Analysis of the ionospheric cross polar cap potential drop using DMSP data during the National Space Weather Program study period, *J. Geophys. Res.*, *103*(A11), 26,337–26,347.

Hairston, M. R., et al. (2003), Observed saturation of the ionospheric polar cap potential during the 31 March 2001 storm, *Geophys. Res. Lett.*, *30*(6), 1325, doi:10.1029/2002GL015894.

Hairston, M. R., et al. (2005), Saturation of the ionospheric polar cap potential during the October–November 2003 superstorms, *J. Geophys. Res.*, *110*, A09S26, doi:10.1029/2004JA010864.

Hanson, W. B., W. R. Coley, R. A. Heelis, N. C. Maynard, and T. L. Aggson (1993), A comparison of in-situ measurements of $\mathbf{E}$ and $-\mathbf{V} \times \mathbf{B}$ from Dynamics Explorer-2, *J. Geophys. Res.*, *98*(A12), 21,501–21,516.

Hapgood, M., and M. Lockwood (1993), On the voltage and distance across the low latitude boundary layer, *Geophys. Res. Lett.*, *20*(2), 145–148.

Holzer, R. E., R. L. McPherron, and D. A. Hardy (1986), A quantitative empirical model of the magnetospheric flux transfer process, *J. Geophys. Res.*, *91*, 3287–3293.

Hones, E. W., Jr., et al. (1989), Horse-collar aurora: A frequent pattern of the aurora in quiet times, *Geophys. Res. Lett.*, *16*(1), 37–40.

Hubert, B., et al. (2006), Dayside and nightside reconnection rates inferred from IMAGE FUV and Super Dual Auroral Radar Network data, *J. Geophys. Res.*, *112*, A03217, doi:10.1029/2005JA011140.

Khan, H., and S. W. H. Cowley (1999), Observations of the response time of high-latitude ionospheric convection to variations in the interplanetary magnetic field using EISCAT and IMP-8 data, *Ann. Geophys.*, *17*(10), 1306–1335.

Kihn, E. A., et al. (2006), A statistical comparison of the AMIE derived and DMSP-SSIES observed high-latitude ionospheric electric field, *J. Geophys. Res.*, *111*, A08303, doi:10.1029/2005JA011310.

King, J. H., and N. E. Papitashvili (2005), Solar wind spatial scales in and comparisons of hourly Wind and ACE plasma and magnetic field data, *J. Geophys. Res.*, *110*(A2), A02209, doi:10.1029/2004JA010804.

Kivelson, M. G., and A. J. Ridley (2008), Saturation of the polar cap potential: Inference from Alfven wing arguments, *J. Geophys. Res.*, *113*, A05214, doi:10.1029/2007JA012302.

Lagarias, J. C., J. A. Reeds, M. H. Wright, and P. E. Wright (1998), Convergence properties of the Nelder-Mead simplex method in low dimensions, *Soc. Ind. Appl. Math. J. Optim.*, *9*(1), 112–147.

Lockwood, M. (1991), On flow reversal boundaries and transpolar voltage in average models of high latitude convection, *Planet. Space Sci.*, *39*, 397–409.

Lockwood, M. (1997), The relationship of dayside auroral precipitations to the open-closed separatrix and the pattern of convective flow, *J. Geophys. Res.*, *102*(A8), 17,475–17,487.

Lockwood, M. (2002a), Relationship between the near-Earth interplanetary field and the coronal source flux: Dependence on timescale, *J. Geophys. Res.*, *107*(A12), 1425, doi:10.1029/2001JA009062.

Lockwood, M. (2002b), An evaluation of the correlation between open solar flux and total solar irradiance, *Astron. Astrophys.*, *382*, 678–687.

Lockwood, M., and S. W. H. Cowley (1988), Observations at the magnetopause and in the auroral ionosphere of momentum transfer from the solar wind, *Adv. Space Res.*, *8*(9/10), 281–299.

Lockwood, M., and S. W. H. Cowley (1992) Ionospheric convection and the substorm cycle, in *Substorms 1, Proceedings of the First International Conference on Substorms, ICS-1*, edited by C. Mattock, *ESA-SP-335, 99-109*, pp. 99–109, Eur. Space Agency Publ., Noordvijk, Netherlands.

Lockwood, M., and M. P. Freeman (1989), Recent ionospheric observations relating to solar wind-magnetosphere coupling, *Philos. Trans. R. Soc. London, Ser. A*, *328*, 93–105.

Lockwood, M., and S. E. Morley (2004), A numerical model of the ionospheric signatures of time-varying magnetic reconnection. I: Ionospheric convection, *Ann. Geophys.*, *22*, 73–91.

Lockwood, M., S. W. H. Cowley, H. Todd, D. M. Willis, and C. R. Clauer (1988), Ion flows and heating at a contracting polar cap boundary, *Planet. Space Sci.*, *36*, 1229–1253.

Lockwood, M., S. W. H. Cowley, and M. P. Freeman (1990), The excitation of plasma convection in the high latitude ionosphere, *J. Geophys. Res.*, *95*(A6), 7961–7972.

Lockwood, M., K. Throp, B. S. Lanchester, S. K. Morley, S. E. Milan, and M. Lester (2006), Modelling the observed proton aurora and ionospheric convection responses to changes in the IMF field clock angle: 2. The persistence of ionospheric convection, *J. Geophys. Res.*, *111*, A02306, doi:10.1029/2003JA010307.

Lu, G., et al. (1994), Interhemispheric asymmetry of the high-latitude ionospheric convection pattern, *J. Geophys. Res.*, *99*(A4), 6491–6510.

Lu, G., et al. (2002a), Ionospheric response to the interplanetary magnetic field southward turning: Fast onset and slow reconfiguration, *J. Geophys. Res.*, *107*(A8), 1153, doi:10.1029/2001JA000324.

Lu, G., et al. (2002b), Solar wind effects on ionospheric convection: A review, *J. Atmos. Sol. Terr. Phys.*, *64*(2), 145–157.

Milan, S. E. (2004), Dayside and nightside contributions to the cross polar cap potential: Placing an upper limit on a viscous-like interaction, *Ann. Geophys.*, *22*(10), 3771–3777.

Milan, S. E., G. Provan, and B. Hubert (2007), Magnetic flux transport in the Dungey cycle: A survey of dayside and nightside reconnection rates, *J. Geophys. Res.*, *112*, A01209, doi:10.1029/2006JA011642.

Milan, S. E., P. D. Boakes, and B. Hubert (2008), Response of the expanding/contracting polar cap to weak and strong solar wind driving: Implications for substorm onset, *J. Geophys. Res.*, *113*, A09215, doi:10.1029/2008JA013340.

Morley, S. K., and M. Lockwood (2005), A numerical model of the ionospheric signatures of time-varying magnetic reconnection. II: Measuring expansions in the ionospheric flow response, *Ann. Geophys.*, *23*, 2501–2510.

Mozer, F. S., H. Hayakawa, S. Kokubun, M. Nakamura, T. Okada, T. Yamamoto, and K. Tsuruda (1994), The morningside low-latitude boundary-layer as determined from electric and magnetic-field measurements on Geotail, *Geophys. Res. Lett.*, *21*(25), 2983–2986.

Murphree, J. S., C. D. Anger, and L. L. Cogger (1982), The instantaneous relationship between polar cap and oval auroras at times of northward interplanetary magnetic field, *Can. J. Phys.*, *60*, 349.

Nagatsuma, T. (2004), Conductivity dependence of cross-polar potential saturation, *J. Geophys. Res.*, *109*(A4), A04210, doi:10.1029/2003JA010286.

Nakata, H., et al. (2004), Ionospheric electric potentials for substorms calculated from a solar wind-magnetosphere MHD simulation and a magnetogram inversion technique, *J. Geophys. Res.*, *109*, A01211, doi:10.1029/2002JA009743.

Nelder, J. A., and R. Mead (1965), A simplex method for function minimization, *Comput. J.*, *7*, 308–313.

Newell, P. T., et al. (2008), Pairs of solar wind-magnetosphere coupling functions: Combining a merging term with a viscous term works best, *J. Geophys. Res.*, *113*, A04218, doi:10.1029/2007JA012825.

Nishida, A. (1983), IMF control of the earth's magnetosphere, *Space Sci. Rev.*, *34*(2), 185–200.

Papitashvili, V. O., and F. J. Rich (2002), High-latitude ionospheric convection models derived from Defense Meteorological Satellite Program ion drift observations and parameterized by the interplanetary magnetic field strength and direction, *J. Geophys. Res.*, *107*(A8), 1198, doi:10.1029/2001JA000264.

Phan, T.-D., M. Oieroset, and M. Fujimoto (2005), Reconnection at the dayside low-latitude magnetopause and its nonrole in low-latitude boundary layer formation during northward interplanetary magnetic field, *Geophys. Res. Lett.*, *32*, L17101, doi:10.1029/2005GL023355.

Provan, G., et al. (2004), Statistical study of high-latitude plasma flow during magnetospheric substorms, *Ann. Geophys.*, *22*, 3607–3624.

Reiff, P. H., and J. G. Luhmann (1986), Solar wind control of the polar-cap voltage, in *Solar Wind-Magnetosphere Coupling*, *Proc. Chapman Conference*, edited by Y. Kamide and J. Slavin, pp. 453–476, Springer, New York.

Reiff, P. H., R. R. Spiro, and T. Hill (1981), Dependence of polar cap potential on interplanetary parameters, *J. Geophys. Res.*, *86*(A9), 7639–7648.

Reiff, P. H., et al. (1985), Comparison of polar-cap potential drops estimated from solar-wind and ground magnetometer data: CDAW-6, *J. Geophys. Res.*, *90*(A2), 1318–1324.

Ridley, A. J. (2005), A new formulation for the ionospheric cross polar cap potential including saturation effects, *Ann. Geophys.*, *23*(11), 3533–3547.

Ridley, A. J., and E. A. Kihn (2004), Polar cap index comparisons with AMIE cross polar cap potential, electric field, and polar cap area, *Geophys. Res. Lett.*, *31*, L07801, doi:10.1029/2003GL019113.

Ruohoniemi, J. M., and R. A. Greenwald (1998), The response of high-latitude convection to a sudden southward IMF turning, *Geophys. Res. Lett.*, *25*(15), 2913–2916.

Ruohoniemi, J. M., and R. A. Greenwald (2005), Dependencies of high-latitude plasma convection: Consideration of interplanetary magnetic field, seasonal, and universal time factors in statistical patterns, *J. Geophys. Res.*, *110*, A09204, doi:10.1029/2004JA010815.

Russell, C. T. (1972), The configuration of the magnetosphere, in *Critical Problems of Magnetospheric Physics*, edited by E. R. Dyer, p. 1, Inter-Union Comm. on Sol. Terr. Phys., Nat. Acad. of Sci., Washington, D. C.

Shepherd, S. G., et al. (2002), Cross polar cap potentials measured with Super Dual Auroral Radar Network during quasi-steady solar wind and interplanetary magnetic field conditions, *J. Geophys. Res.*, *107*(A7), 1094, doi:10.1029/2001JA000152.

Siscoe, G. L., and T. S. Huang (1985), Polar cap inflation and deflation, *J. Geophys. Res.*, *90*(A1), 543–547.

Siscoe, G. L., W. Lotko, and B. U. O. Sonnerup (1991), A high-latitude, low-latitude boundary-layer model of the convection current system, *J. Geophys. Res.*, *96*(A3), 3487–3495.

Siscoe, G., et al. (2004), Transpolar potential saturation models compared, *J. Geophys. Res.*, *109*, A09203, doi:10.1029/2003JA010318.

Sonnerup, B. U. O., et al. (2001), Simulations of the magnetosphere for zero interplanetary magnetic field: The ground state, *J. Geophys. Res.*, *106*(A12), 29,419–29,434.

Weimer, D. R. (1999), Substorm influence on the ionospheric electric potentials and currents, *J. Geophys. Res.*, *104*(A1), 185–197.

Weimer, D. R. (2001), An improved model of ionospheric electric potentials including substorm perturbations and application to the Geospace Environment Modeling November 24, 1996, event, *J. Geophys. Res.*, *106*(A1), 407–416.

Wygant, J. R., R. B. Torbert, and F. S. Mozer (1983), Comparison of S3-3 polar cap potential drops with the interplanetary magnetic field and models of magnetopause reconnection, *J. Geophys. Res.*, *88*(A7), 5727–5735.

Zhang, S. R., et al. (2007), High latitude convection based on long-term incoherent scatter radar observations in North America, *J. Atmos. Sol. Terr. Phys.*, *69*(10-11), 1273–1291.

I. Finch, Space Science and Technology Department, Rutherford Appleton Laboratory, Chilton, Didcot, OX11 0QX, Oxfordshire, UK. (I.D.Finch@rl.ac.uk)

M. Hairston, W. B. Hanson Center for Space Sciences, University of Texas at Dallas, P.O. Box 830688 FO22 Richardson, TX 75083-0688, USA. (hairston@utdallas.edu)

M. Lockwood, Space Science and Technology Department, Rutherford Appleton Laboratory, R-25, Room 1-04, Chilton, Didcot OX11 0QX, UK. (m.lockwood@rl.ac.uk)

A. Rouillard, Space Environment Physics, School of Physics and Astronomy, Southampton University, Highfield, Southampton, SO17 1BJ, Hampshire, UK. (alexisrouillard@yahoo.co.uk)